



HAL
open science

A global analysis of the asymmetric effect of ENSO on extreme precipitation

X. Sun, Benjamin Renard, M. Thyer, S. Westra, M. Lang

► **To cite this version:**

X. Sun, Benjamin Renard, M. Thyer, S. Westra, M. Lang. A global analysis of the asymmetric effect of ENSO on extreme precipitation. *Journal of Hydrology*, 2015, 530, pp.51-65. 10.1016/j.jhydrol.2015.09.016 . hal-01700741

HAL Id: hal-01700741

<https://hal.science/hal-01700741>

Submitted on 5 Feb 2018

HAL is a multi-disciplinary open access archive for the deposit and dissemination of scientific research documents, whether they are published or not. The documents may come from teaching and research institutions in France or abroad, or from public or private research centers.

L'archive ouverte pluridisciplinaire **HAL**, est destinée au dépôt et à la diffusion de documents scientifiques de niveau recherche, publiés ou non, émanant des établissements d'enseignement et de recherche français ou étrangers, des laboratoires publics ou privés.

1 **A global analysis of the asymmetric effect of ENSO on extreme precipitation**

2 Xun SUN¹, Benjamin RENARD², Mark THYER³, Seth WESTRA³, Michel LANG²

3

4 Correspondence to: Dr. X. Sun.

5 E-mail address: xs2226@columbia.edu

¹ Columbia Water Center, Columbia University, New York, NY 10027, USA

² Irstea, UR HHLY, centre de Lyon-Villeurbanne, F-69626 Villeurbanne, France

³ School of Civil, Environmental & Mining Engineering, University of Adelaide, SA, 5005,
Australia

6 *Abstract*

7 The global and regional influence of the El Niño-Southern Oscillation (ENSO) phenomenon on
8 extreme precipitation was analyzed using a global database comprising over 7000 high quality
9 observation sites. To better quantify possible changes in relatively rare design-relevant precipitation
10 quantiles (e.g. the 1 in 10 year event), a Bayesian regional extreme value model was used, which
11 employed the Southern Oscillation Index (SOI) – a measure of ENSO – as a covariate. Regions
12 found to be influenced by ENSO include parts of North and South America, southern and eastern
13 Asia, South Africa, Australia and Europe. The season experiencing the greatest ENSO effect varies
14 regionally, but in most of the ENSO-affected regions the strongest effect happens in boreal winter,
15 during which time the 10-year precipitation for $|\text{SOI}|=20$ (corresponding to either a strong El Niño
16 or La Niña episode) can be up to 50% higher or lower than for $\text{SOI}=0$ (a neutral phase).
17 Importantly, the effect of ENSO on extreme precipitation is asymmetric, with most parts of the
18 world experiencing a significant effect only for a single ENSO phase. This finding has important
19 implications on the current understanding of how ENSO influences extreme precipitation, and will
20 enable a more rigorous theoretical foundation for providing quantitative extreme precipitation
21 intensity predictions at seasonal timescales. We anticipate that incorporating asymmetric impacts of
22 ENSO on extreme precipitation will help lead to better-informed climate-adaptive design of flood-
23 sensitive infrastructure.

24

25 **Keywords:** ENSO, asymmetric relationship, extreme precipitation, Bayesian regional modeling, GEV
26 distribution, climate-informed model

27

28 1 INTRODUCTION

29 Every year, extreme precipitation results in flooding that leads to loss of life and infrastructure, as
30 well as economic disruption. Not only are the direct effects of floods felt for many years, but the
31 indirect effects - including disease, trauma and social dislocation, reduced agricultural production or
32 loss of manufacturing capacity - can be felt for decades (Ahern et al., 2005). The El Niño-Southern
33 Oscillation (ENSO) is the single most influential climate phenomenon affecting the variability of
34 global precipitation extremes (Dai et al., 1997), and understanding the ENSO-extreme precipitation
35 relationship is therefore critical to predict and manage the impacts of floods at global and regional
36 scales (Ward et al., 2014a; Ward et al., 2014b). While many previous studies have detected the
37 ENSO impact on extreme precipitation indices, this study is the first to undertake a global analysis
38 that quantifies the asymmetric impact of ENSO on “design-relevant” extreme precipitation
39 quantiles (e.g. the 1 in 10 year event).

40

41 A large number of studies have discussed the relationship between the two ENSO phases (El Niño
42 and La Niña) and regional average precipitation. Ropelewski and Halpert (1987) provided a global
43 pattern of the magnitude, phase and duration of ENSO-related precipitation. Dai et al. (1997) and
44 Dai and Wigley (2000) also examined precipitation over the oceans and described a global pattern
45 of the effect of ENSO on precipitation. In boreal winter, positive anomalies occur in southwestern
46 North America during El Niño episodes and northwestern North America during La Niña episodes
47 (Castello and Shelton, 2004; Meehl et al., 2007). Positive anomalies occur during El Niño episodes
48 in southeastern South America in austral winter, spring and summer, and northeastern South
49 America in autumn (Fernandez and Fernandez, 2002; Grimm, 2011; Kayano and Andreoli, 2006).
50 La Niña enhances the rainfall in South Africa in summer (Kruger, 1999; Vanheerden et al., 1988),

51 and significant effects are also found in Asia (Kane, 1999; Kripalani and Kulkarni, 1997; Li and
52 Ma, 2012; Wu et al., 2003) and Australia (Cai and Cowan, 2009).

53

54 Although many of the early studies of the ENSO-precipitation relationship focus on seasonal and
55 annual average precipitation, an increasing number of studies have begun to focus on the
56 relationship between ENSO and extreme precipitation, given its importance in understanding flood
57 risk. For instance, a significant ENSO influence was found on the frequency of extreme
58 precipitation in North America (Cayan et al., 1999; Gershunov and Barnett, 1998; Higgins et al.,
59 2011; Jones and Carvalho, 2012; Schubert et al., 2008) and South America (Grimm and Tedeschi,
60 2009; Pscheidt and Grimm, 2009). This relationship had also been studied in China (Wan et al.,
61 2013) and Australia (Min et al., 2013). At the global scale, Curtis et al. (2007) investigated the
62 correlation between ENSO and the frequency of estimated precipitation extremes for different
63 seasons, while Lyon and Barnston (2005) discussed the spatial extent of tropical land precipitation
64 extremes related to the extreme phases of ENSO. Kenyon and Hegerl (2010) reported on the
65 response of global extreme precipitation to ENSO. Alexander et al. (2009) studied the global
66 response of precipitation extremes to global sea surface temperature variability.

67

68 A limitation of many of these studies is that the “extremes” investigated are still relatively frequent
69 events, and thus not directly meaningful from a flood risk estimation perspective. For example,
70 Cayan et al. (1999) used the daily precipitation larger than the 90th percentiles (P90), while Lyon
71 and Barnston (2005) used an index based on monthly precipitation anomalies from a gridded
72 dataset. In contrast, the design, management and operation of water-related engineering
73 infrastructure often requires information on rarer “design-relevant” extremes, such as the 1 in 10
74 year or 1 in 100 year precipitation event (Westra et al., 2014). The rarity of such events makes
75 detecting an association between extreme rainfall and ENSO difficult, and a framework for

76 quantifying such effects is therefore required to assist with the design and operation of engineering
77 systems that can adapt to ENSO-induced climate variability.

78

79 To move beyond simply detecting the ENSO effect on extreme precipitation indices and instead
80 focus on estimating ENSO effect on extreme precipitation quantiles that are “design-relevant”, one
81 needs to account for the specific features of extreme precipitation. Challenges with estimating
82 extreme precipitation quantiles include:

- 83 1. At-site extremes are much more variable than temporally or spatially averaged precipitation.
84 As a consequence, detecting an ENSO effect is more difficult due to a lower signal-to-noise
85 ratio, which raises questions on the ability of local methods to detect ENSO effects;
- 86 2. Extreme precipitation usually occurs over a small spatial area within a short time. Thus,
87 spatially smoothed datasets, such as gridded datasets, are not well-adapted. As an illustration,
88 Mannshardt-Shamseldin et al. (2010) showed that raingauge-based precipitation quantiles
89 may be two to three times higher than gridded precipitation quantiles. However, the use of
90 raingauge-based data poses specific difficulties in terms of irregular spatial sampling and
91 handling of missing data; and
- 92 3. Quantifying ENSO effects on extreme precipitation requires use of appropriate probabilistic
93 models (i.e. extreme value distributions).

94

95 To analyze and predict the impact of climate variability on extreme hydrological variables, several
96 non-stationary and climate-informed frequency analysis (FA) models have been developed at both
97 local scale (e.g. Renard et al. (2006b), Kwon et al. (2008), Ouarda and El-Adlouni (2011),
98 Trambly et al. (2012)) and regional scale (e.g. Renard et al. (2006a), Hanel et al. (2009), Aryal et
99 al. (2009), Lima and Lall (2010b), Shang et al. (2011), Westra and Sisson (2011)). Local analyses
100 generally lead to large uncertainties that may mask the ENSO effect. Although regional analyses

101 may improve the detection power, additional difficulties are induced by the inherent spatial
102 structure of precipitation. Furthermore, most of the aforementioned regional studies ignore spatial
103 dependence (an exception being Westra and Sisson (2011)).

104

105 Another limitation of many previous studies that describe the ENSO-precipitation teleconnection is
106 that they often assumed a symmetric relation (with anomalies during El Niño being the opposite of
107 those during La Niña (Hoerling et al., 1997)), however this assumption is increasingly being
108 questioned. Several studies have demonstrated asymmetric associations between ENSO and climate
109 variables (e.g., pressure and precipitation) (Hannachi, 2001; Hoerling et al., 2001; Hoerling et al.,
110 1997; OrtizBevia et al., 2010; Sardeshmukh et al., 2000). Asymmetry has been reported for the
111 ENSO effect on regional rainfall for the winter precipitation response in North America by Wu et
112 al. (2005), and for the spring rainfall in south China and Taiwan by Feng and Li (2011) and Chen et
113 al. (2008). In Australia, the asymmetric effect of ENSO on extreme precipitation has been described
114 for southeast Queensland (Cai and van Rensch, 2012; Cai et al., 2010; Sun et al., 2014) and eastern
115 Australian regions (King et al., 2013). Importantly, Sun et al. (2014) showed that, compared to the
116 asymmetric ENSO-precipitation model, the assumption of either no ENSO effect or only a
117 symmetric ENSO-precipitation relationship led to a strong underestimation of extreme precipitation
118 quantiles in southeast Queensland during La Nina episodes. This has significant practical
119 implications for the design and management of flood-sensitive engineering infrastructure. Hence,
120 there is a clear need to develop a global perspective on the form of the extreme ENSO-precipitation
121 relationship, in particular for extreme precipitation quantiles.

122

123 This study provides the first quantitative assessment of the global asymmetric effect of ENSO on
124 seasonal “design-relevant” extreme daily precipitation. We extend the study of Sun et al. (2014) to a
125 new global high quality gauge-based observation dataset (HadEX2) comprising observations at over

126 7000 stations (Donat et al., 2013). The same climate-informed Bayesian regional frequency analysis
127 (RFA) method that was developed in Sun et al (2014) is applied to analyze the at-site extremes
128 across this larger spatial domain. This method enables detecting and quantifying the effect of
129 climate variability on extreme precipitation with the consideration of spatial dependence, and can
130 account for situations where records at each site are of different lengths and contain missing values.
131 Furthermore, the fact that ENSO effects are regionalized yields more precise estimates of the
132 ENSO-extreme precipitation relationship compared to at-site analysis, while also providing
133 sufficient resolution to identify distinct regional features. We apply this regional frequency analysis
134 approach to geographic regions covering all land areas. The contribution is highlighted from the
135 perspective of engineering design, which requires considering at-site extremes, rather than spatially
136 smoothed gridded data sets. This makes the key difference with other studies that analyzed the
137 relationship between ENSO and extreme precipitation at a large scale.

138

139 This paper is organized as follows. Section 2 presents the dataset and briefly outlines the climate-
140 informed RFA framework applied to extreme precipitation. Section 3 assesses several assumptions
141 made by the RFA model and justifies its application on the global data set. Section 4 describes the
142 main results of the analysis, including the ENSO effect on extreme precipitation and the possible
143 asymmetry of this effect. Practical implications and further improvements are discussed in Section
144 5. Section 6 summarizes the main findings of the study.

145 **2 DATA AND METHOD**

146 **2.1 Data**

147 The Hadley Center Global Climate Extremes Index 2 (HadEX2) dataset (Donat et al., 2013)
148 comprises the monthly maxima of daily precipitation from 11,588 high quality observation sites

149 (Figure 1). The 7037 sites with records longer than 40 years were used, with a median record length
150 of 60 years. The highest density of gauges is in Europe, the United States and South Africa, and the
151 lowest density is in Amazonia, most of Africa, central Asia, tropical areas of Asia and central
152 Australia. Overall, temperate climate areas are much more represented than tropical or subtropical
153 ones, while polar areas are very scarcely gauged. For each site, we calculated the seasonal maxima
154 of daily precipitation for December-January-February (DJF), March-April-May (MAM), June-July-
155 August (JJA) and September-October-November (SON).

156

157 The Southern Oscillation Index (SOI) is a measure of the strength of ENSO. The index is calculated
158 from the monthly mean sea level pressure difference between Tahiti and Darwin. Typically, as
159 presented in the website of Australian Bureau of Meteorology (BOM) (<http://www.bom.gov.au/>
160 [climate/glossary/soi.shtml](http://www.bom.gov.au/climate/glossary/soi.shtml)), sustained negative SOI values below about -8 indicate an El Niño event
161 while sustained positive values above $+8$ indicate a La Niña event, although for simplicity we refer
162 to a negative value of the SOI as an El Niño and a positive value as a La Niña. The SOI data (1877-
163 2011) used in this study were obtained from the BOM website, and were seasonally averaged using
164 the same seasons as for precipitation.

165 **2.2 A regional extreme value model**

166 We apply a climate-informed regional frequency analysis (RFA) method to evaluate the effect of
167 ENSO on extreme precipitation. This framework includes: (1) A generalised extreme value (GEV)
168 model for extreme precipitation; (2) GEV parameters dependent on covariates based on indices of
169 ENSO (SOI); (3) Spatial dependence represented by a Gaussian copula; (4) Bayesian inference
170 techniques to provide reliable estimates of parameter and predictive uncertainty. Reliable estimates
171 of parameter uncertainty are essential for models of extremes precipitation because the data lengths
172 are short and the parameter uncertainty is a significant component of the predictive uncertainty.

173 A complete presentation of the method along with comparisons of alternative model formulations is
 174 given by Sun et al. (2014), and the methodology is summarized briefly here.

175 **2.2.1 Probabilistic regional model**

176 The generalized extreme value (GEV) distribution (Fisher and Tippett, 1928) is often used to
 177 describe the distribution of annual or seasonal maxima. The cumulative distribution function (cdf)
 178 of the GEV distribution is:

$$179 \quad G(y | \mu, \sigma, \xi) = \exp \left(- \left[1 - \xi \left(\frac{y - \mu}{\sigma} \right) \right]^{\frac{1}{\xi}} \right) \quad (1)$$

180 where μ , σ and ξ are the location, scale and shape parameters, respectively. In the following, we call
 181 these three parameters the D-parameters (i.e., distribution parameters).

182

183 For a given region, the observed seasonal maximum at site s and time t is a realization from the
 184 random variable $Y(s, t)$. To develop the regional model, a GEV distribution is assumed for all sites
 185 (Coles et al., 2003; Katz et al., 2002) with D-parameters allowed to vary in both space and time:

$$186 \quad Y(s, t) \sim GEV(\mu(s, t), \sigma(s, t), \xi(s, t)) \quad (2)$$

187 For each D-parameter, a regression function is used to link the parameter value with the temporally-
 188 varying covariate SOI. Following Sun et al. (2014), a piecewise linear regression function for the
 189 location and scale parameters is used to separately evaluate the effect of ENSO during the El Niño
 190 and La Niña phases. We do not assume any ENSO-related regression functions for the shape
 191 parameter since this parameter is difficult to estimate even in a stationary context (Coles, 2001,
 192 p106).

193

194 Because ENSO is a large-scale (global) mode of variability, we reason that the influence of ENSO
 195 on precipitation would be a slowly varying function in space, and have therefore assumed that some

196 regression parameters would be constant for all sites within a geographic region (defined in Section
 197 2.2.2). This regional approach results in reduced uncertainty of parameters and predictions relative
 198 to estimating parameters separately at each gauge, as had been demonstrated in a number of
 199 previous studies (e.g., Renard et al. (2006a); Hanel et al. (2009); Westra and Sisson (2011); Sun et
 200 al. (2014)).

201

202 The regression function for each D-parameter is therefore given by:

$$203 \quad \mu(s, t) = \begin{cases} \mu_{loc_0}^{(s)} + \mu_{reg_1}^- * SOI(t); & SOI(t) < 0, \text{ El Ni ño} \\ \mu_{loc_0}^{(s)} + \mu_{reg_1}^+ * SOI(t); & SOI(t) > 0, \text{ La Ni ña} \end{cases} \quad (3a)$$

$$204 \quad \sigma(s, t) = \begin{cases} \sigma_{loc_0}^{(s)} + \sigma_{reg_1}^- * SOI(t); & SOI(t) < 0, \text{ El Ni ño} \\ \sigma_{loc_0}^{(s)} + \sigma_{reg_1}^+ * SOI(t); & SOI(t) > 0, \text{ La Ni ña} \end{cases} \quad (3b)$$

$$205 \quad \xi(s, t) = \xi_{reg} \quad (3c)$$

206 We denote $\theta_{loc}^{(s)} = (\mu_{loc_0}^{(s)}, \sigma_{loc_0}^{(s)})$ and $\theta_{reg} = (\mu_{reg_1}^-, \mu_{reg_1}^+, \sigma_{reg_1}^-, \sigma_{reg_1}^+, \xi_{reg})$ as regression parameters that
 207 need to be estimated. $\theta_{loc}^{(s)}$ are site-specific (local) parameters, while θ_{reg} are regional parameters
 208 which are common for all sites within the region. The use of piecewise linear regression functions
 209 outlined in Eq. (3), with different linear functions in the El Ni ño and La Ni ña phases, enables the
 210 modelling framework to capture and evaluate the asymmetric nature of the ENSO-precipitation
 211 relationship.

212

213 Spatial dependence between data inside a region is described with a Gaussian copula as used in Sun
 214 et al. (2014). The dependence matrix Σ for the Gaussian copula is:

$$215 \quad \Sigma(s_i, s_j) = \eta_1 \exp(-\eta_2 * \|s_i, s_j\|) \quad (4)$$

216 where $\|s_i, s_j\|$ is the distance between sites s_i and s_j , and $\eta = (\eta_1, \eta_2)$ are two parameters to be
 217 estimated.

218 Explicitly representing spatial dependence in this way is important to accurately characterize
219 uncertainty (e.g. Westra and Sisson (2011)), since nearby gauges often show high levels of statistical
220 dependence. The Gaussian copula is a member of the elliptical copulas family (which also
221 comprises the Student copula), which remains applicable to high-dimension models such as here (a
222 region can comprise up to 16 sites, see next section) (Renard, 2011). More detailed discussions on
223 the use of the Gaussian copula can be found in Favre et al. (2004); Renard and Lang (2007); Renard
224 et al. (2013), and details on likelihood function computation can be found in Sun et al. (2014). We
225 also discuss the limitation of this approach in the discussion Section 5.4.

226 2.2.2 Defining regions

227 Regional analyses reduce sampling uncertainty compared to at-site (local) analyses. However, to
228 obtain the spatial pattern of the ENSO effect, regions should be neither too small nor too large:
229 small regions may not contain enough sites to precisely estimate the model parameters, while large
230 regions may not have a consistent association with the SOI. Therefore, we prepared 2592 gridded
231 regions with a grid size of 5° by 5° (about 309,000 km² at the equator and 155,000 km² at 60°N),
232 and applied the regional model described in Section 2.2.1 to each region. Note that this regional
233 model does not assume that the distribution of extreme precipitation is constant within each region.
234 It only assumes that the strength of the ENSO effect and the shape parameter are constant. However,
235 the local parameters $\theta_{loc}^{(s)} = (\mu_{loc_0}^{(s)}, \sigma_{loc_0}^{(s)})$ enable variability in the GEV distribution within each region,
236 with the location and scale parameters of the GEV distribution remaining site-specific.

237

238 To keep computation time feasible, we used only some of the available observation sites in a region
239 (the computational bottleneck being the inversion of the dependence matrix Σ). Site selection was
240 achieved by subdividing each region into 16 sub-regions, from which the gauge with the longest
241 record was selected if there is more than one gauge available (red dots in Figure 2). Therefore, in

242 each region, there were at most 16 sites used for regional analysis. We considered a region to
243 possess enough data to apply the regional model if there were at least three sub-regions with
244 available gauges. In total, there are 323 regions that meet the requirement of station number and
245 record length. A justification of this way of defining regions will be described in Section 3.1.

246 **2.2.3 Inference**

247 For each region, we estimated the parameters θ in a Bayesian framework using the Markov chain
248 Monte Carlo (MCMC) method. Relevant formulae can be found in Sun et al. (2014). In the current
249 study, non-informative priors were used (but see Section 3.1.4 for an evaluation of an informative
250 prior on the shape parameter). More details about the MCMC sampler are described by Renard et al.
251 (2006a). To ensure convergence, we ran two chains with different starting points for each region.
252 The Gelman-Rubin (GR) index (Gelman and Rubin, 1992) was used, and the MCMC sampling was
253 considered as convergent when the GR value was less than 1.2 for all parameters. Note that the use
254 of Bayesian inference allows the effect of sampling uncertainty to be quantified for all inferred
255 quantities. The results are therefore not restricted to point-estimates of quantities such as the ENSO
256 effect, conditional quantiles, and so on, but also encompass the associated uncertainties.

257 The Bayesian approach is not the only possible way to estimate parameters and their uncertainties.
258 Likelihood-based methods (Bayesian or maximum likelihood) are generally favored over moment-
259 based methods when covariates are used in the model as done here: indeed, the inclusion of the
260 covariates in the likelihood function is quite straightforward, while deriving theoretical moments for
261 given realizations of the covariates is more challenging. Maximum likelihood estimation techniques
262 could also be used to estimate parameters and their uncertainty (e.g. using asymptotic Gaussian
263 approximations or bootstrap, see Frey and Burmaster (1999)). However, we favored the Bayesian
264 framework because it could be more adapted for future improvements of the statistical model we

265 consider (e.g. using region-specific priors, hierarchical modeling, etc.). This will be further
266 discussed in section 5.4.

267 2.2.4 The effect of ENSO on precipitation quantiles

268 The effect of ENSO on precipitation quantiles is presented by calculating the slope of the SOI-
269 quantile relationship. More precisely, for a given exceedance probability $1-\alpha$, the associated
270 quantile q_α is computed through the inverse function of Eq. (1):

$$271 \quad q_\alpha = \frac{\sigma}{\xi} K_\alpha + \mu \quad (5)$$

272 where $K_\alpha = 1 - (-\log(\alpha))^\xi$.

273 By applying Eq. (3) to each D-parameter conditional on a specific SOI value, the quantile q_α of site
274 s becomes:

$$275 \quad q_\alpha(s) = \mu_{loc_0}^{(s)} + \frac{\sigma_{loc_0}^{(s)}}{\xi_{reg}} K_\alpha + slp_\alpha * SOI \quad (6)$$

276 where $slp_\alpha = \begin{cases} \mu_{reg_1}^- + \frac{\sigma_{reg_1}^-}{\xi_{reg}} K_\alpha; SOI < 0 \\ \mu_{reg_1}^+ + \frac{\sigma_{reg_1}^+}{\xi_{reg}} K_\alpha; SOI > 0 \end{cases}$ is the slope of the quantile with respect to the SOI. Note that

277 as the slope slp_α only depends on the regional parameters, it is itself regional and hence does not
278 depend on site s within a given region.

279 3 MODEL ILLUSTRATION AND VERIFICATION

280 To assess the validity of the main model assumptions and to verify that the strategy used to define
281 regions and to select the stations within each region is relevant, we start our analysis by focusing on
282 a particular region. We consider a region at mid to low latitude with a relatively large geographic

283 area to verify whether using sixteen stations is enough to obtain stable estimates. According to the
284 coverage and availability of the data, we select the region at 32.5N 100W in Southern US (Figure
285 2).

286 **3.1 Model demonstration for a particular region**

287 **3.1.1 Goodness of fit**

288 We applied the regional model described in Eq. (3) to the DJF maximum precipitation of the sixteen
289 stations shown as red dots in Figure 2. The goodness-of-fit of the time-varying GEV distribution
290 can be verified through a probability-probability plot (pp-plot). For a given site s , the pp-plot is
291 obtained by computing the cdfs $\{\hat{G}_{s,t}(y(s,t))\}_{t=1,n}$ where t indicates the time step, $\hat{G}_{s,t}$ is the cdf of
292 the estimated time-varying GEV at time t , and $y(s,t)$ is the corresponding observation. For a good
293 fit, these cdf values should be realizations from Unif[0,1] distribution, yielding a pp-plot close to
294 the diagonal (see e.g. Renard et al. (2013) and Sun et al. (2014) for more details). Figure S1 (a)
295 shows a good fit for most stations. To further verify the goodness-of-fit, a Kolmogorov-Smirnov
296 test (KS-test) at 0.05 level was used to test the distribution of the cdf values for all sixteen stations
297 against a Unif[0,1] distribution. No significant departure from uniformity was detected, indicating
298 that the model provides an acceptable fit to the observations.

299 **3.1.2 Gaussian copula and exponential dependence-distance model**

300 With the Gaussian copula, the spatial dependence is described through Gaussian-transformed data,
301 where the observation is firstly transformed to a probability by applying the cumulative density
302 function of the marginal GEV distribution, followed by the application of the quantile function of
303 standard Gaussian distribution to obtain the Gaussian-transformed data (see Renard et al. (2013) for
304 the details of data transformation). The empirical dependence of two stations is described by the

305 Pearson correlation coefficient of the Gaussian-transformed data. Figure S1(b) shows the
306 dependence-distance relationship for the Gaussian-transformed data.

307

308 The pairwise Pearson correlations of the observed data show that for the distance of 300 km, the
309 correlation is about 0.4, which corresponds to a rather large decorrelation distance, suggesting that
310 the daily extreme precipitation in this region is created by large-scale atmospheric systems. If this
311 correlation is ignored, the information content of the data will be over-estimated and the uncertainty
312 will be under-estimated. The red lines in Figure S1(b) show that the exponential model (Eq.(4))
313 gives a reasonable approximation of the shape of the dependence-distance relationship. The
314 assumption that the dependence between stations is explained by inter-station distance alone may
315 require further enhancements in some regions (e.g. in mountainous/coastal areas, elevation/distance
316 from coast may also be important) – this is discussed in Section 5.4. However, incorporating some
317 form of spatial dependence still constitutes an improvement over the standard approach that ignores
318 spatial dependence.

319 3.1.3 Stations selection

320 This section assesses whether using 16 stations provides sufficient data to precisely estimate the
321 parameters of the regional model. To this end, we sort the 16 stations in descending order according
322 to their record length, and run the same regional model by using between one to sixteen stations,
323 and compare the posterior distribution of the regional parameters ($\mu_{reg_1}^-$, $\mu_{reg_1}^+$ and ξ) using box
324 plots. Figure S2 shows that when the number of stations is less than three, the posteriors
325 distributions have low precision (large uncertainties). As the number of stations increases, the
326 precision increases (smaller uncertainties), which highlights the advantage of regional analysis
327 compared with local (single station) analysis on providing more precise estimates. When the
328 number of stations is larger than ten, the posterior distributions stabilize, with the boxplots showing

329 very little change both in terms of location and width. This stabilization of the posterior distribution
330 highlights the advantage of modelling spatial dependence: indeed, if the spatial dependence was
331 ignored, each new station would be considered as bringing a similar amount of information, and the
332 estimation uncertainty would mistakenly continue to decrease when the number of stations
333 increases.

334

335 The analysis outlined above was repeated for 1-2 regions in each continent using all available data
336 from those regions, and the results were consistent (not shown). Overall, this highlights two key
337 points: (1) a minimum of approximately three stations is required; and (2) the additional
338 information gain from including more than ten stations in the analysis is fairly limited. Given that
339 the computation burden increases with the number of stations (due to inversion of the covariance
340 matrix), a maximum of sixteen stations was chosen for the remaining analysis of this study.

341 **3.1.4 GEV shape parameter**

342 As the shape parameter is usually difficult to estimate, some expert prior can be used for this
343 parameter. For example, Martins and Stedinger (2000) proposed a Gamma(6,9) distribution
344 (referred to henceforth as the ‘MS prior’) as a general-purpose prior for the shape parameter in a
345 hydrological context. In this study, we also investigate the impact of this prior distribution by
346 comparing estimates obtained with the MS prior and with a non-informative prior (last two boxes of
347 Figure S2). The difference between these two estimates is very small, suggesting that the MS prior
348 does not exert any noticeable leverage on the inference. The MS prior was originally introduced in a
349 local analysis, and in that case expert prior information can markedly improve the estimation.
350 However, in a regional analysis, the MS prior adds less additional information, because the
351 information provided by several stations dominates that provided by the expert prior. We therefore
352 retain the use of non-informative priors when applying the model to the complete dataset.

353 3.2 Verification of the inference for all regions

354 The analysis exemplified in section 3.1 has to be repeated for more than 300 regions, but it is not
355 feasible to manually scrutinize all regions with such a high level of detail. This section therefore
356 describes indicators aimed at verifying that the inference results remain reasonable on the whole
357 dataset.

358

359 Over the 323 regions meeting the data requirement, we first excluded the dry regions with mostly
360 zero values for seasonal maximum precipitation. Then, we estimated the model parameters (Eq.(3))
361 in all remaining regions (see Table 1). Goodness-of-fit was assessed with a KS test (0.05 level)
362 applied on each site. Since the test is repeated for all stations within a given region, we expect to
363 reject the “good-fit” assumption in a percentage of sites close to the error level of the test. It is
364 therefore necessary to assess significance at the regional scale, i.e. to determine which sites show a
365 poor fit, knowing that the local tests have been repeated over all sites of the region. To this end, we
366 used the false discovery rate (FDR) procedure (Benjamini and Hochberg, 1995). Given a regional
367 significance level, we calculated the FDR probability for each region based on the p values of local
368 tests. A region is considered to have a “poor-fit” if the p value of any local test is smaller than the
369 FDR probability. A more detailed description of the FDR procedure in the hydro-climate context is
370 given by Ventura et al. (2004) and Renard et al. (2008). Table 1 shows that the goodness of fit is
371 acceptable in more than 99% of the regions for a regional significance level of 0.05.

372

373 To check the performance of the Gaussian copula in modelling spatial correlation, we can verify
374 whether it provides a better estimation of joint probabilities of exceedances than an equivalent
375 model that ignores spatial dependence. We therefore compute the probability of a station pair
376 jointly exceeding the 75th percentile of the at-site historical seasonal maximum daily precipitation
377 among the stations in a region. We repeatedly calculated this probability for all effective station

378 pairs (defined as a pair with their inter-site distance smaller than 200 km and with at least 20
379 common years without missing values) with both models over all regions. Figure S3 shows the
380 scatterplot of this probability and it indicates that the exceedance probability calculated by the
381 Gaussian copula model is mostly consistent with the empirical probability, while the model
382 ignoring the spatial dependence tends to under-estimate the joint exceedance probability when it
383 becomes large. Therefore, the Gaussian copula model has a better performance than the model
384 ignoring spatial dependence.

385 4 RESULTS

386 In this section, we first describe the results of the parameter inference (Section 4.1). Section 4.2
387 then describes the effect of ENSO on precipitation quantiles. Section 4.3 discusses the seasonal
388 effect of ENSO and Section 4.4 presents the asymmetric effect of ENSO.

389 4.1 Regional parameter estimates

390 In the piecewise linear model proposed in Eq.(3), slope regression parameters $\mu_{reg_1}^-$ and $\sigma_{reg_1}^-$
391 ($\mu_{reg_1}^+$ and $\sigma_{reg_1}^+$) characterize the effect of El Niño (La Niña) on the location and scale parameters. If
392 the effect is significant, the posterior distribution of $\mu_{reg_1}^-$ and/or $\sigma_{reg_1}^-$ ($\mu_{reg_1}^+$ and/or $\sigma_{reg_1}^+$) should be
393 significantly different to zero.

394

395 Figure 3 illustrates significance and intensity for $\mu_{reg_1}^-$ (El Niño) and $\mu_{reg_1}^+$ (La Niña) for each region
396 during DJF. The location parameter increases during a El Niño phase in central and southern North
397 America, southeast South America, southeast China and northern Europe, and decreases in western
398 North America and northern Southeast Asia, and more weakly in South Africa. Conversely, the
399 location parameter increases during a La Niña phase in central North America, northern Southeast

400 Asia, South Africa, Australia and northern Europe, and decreases in southern North America and
401 the northern India subcontinent.

402

403 This global pattern for both phases is consistent with the results of Kenyon and Hegerl (2010) for
404 their November to April season. However, since their study was based on at-site (local) analysis, the
405 significance of the ENSO effect in their results was lower. Our result is also consistent with the
406 ENSO-precipitation teleconnection identified in several regional studies: North America (Castello
407 and Shelton, 2004; Cayan et al., 1999); South America (Grimm and Tedeschi, 2009); eastern China
408 (Wu et al., 2003); and Australia (Cai et al., 2010; King et al., 2013).

409

410 The effect of ENSO on the scale parameter (Figure 4) is also significant in many places, although
411 less than for the location parameter. This important result suggests that ENSO not only shifts the
412 distribution of extremes, but also modifies its variability. In general, for the areas where the effect
413 of ENSO is strong on the location parameter, a similar effect is found on the scale parameter (e.g.
414 southeast China and southeast South America during El Niño; and northern Southeast Asia and
415 Australia during La Niña).

416

417 According to the spatial pattern of the ENSO effect and the availability of data, nineteen areas are
418 defined (Figure 1), with areas 1-4 in Central and North America (Group I), 5-8 in Europe (Group II),
419 9-13 in Asia (Group III), and 14-19 covering the Southern Hemisphere (Group IV). Table 2
420 summarizes the results discussed above for DJF, and also for the three other seasons whose results
421 are not reported in full detail here. It indicates that DJF is the season with the strongest ENSO
422 effect. More detailed results on the seasonality of ENSO effects will be discussed in Section 4.3.

423 4.2 The effect of ENSO on precipitation quantiles

424 A more impact-oriented picture of the effect of ENSO on extreme precipitation can be obtained by
425 expressing it in terms of quantiles rather than in terms of location and scale parameters, as this
426 quantity provides direct information on the likely implications of ENSO on hydrologic hazard. We
427 now show the percentage change in 1 in 10 year DJF precipitation during a strong El Niño or La
428 Niña phase and a neutral phase. The 1 in 10 year precipitation intensity (0.9 quantile) is computed
429 from Eq. (6) with α equal to 0.1, which requires the use of local regression parameters ($\mu_{loc_0}^{(s)}$ and
430 $\sigma_{loc_0}^{(s)}$). Consequently, the estimates from the regional model in terms of quantile change cannot be
431 shown at the scale of regions, but instead has to be shown for all sites. Moreover, note that we can
432 derive the full posterior distribution of this percentage change by propagating all MCMC-generated
433 parameters through Eq. (6).

434

435 Figure 5 illustrates the percentage change for 1 in 10 year precipitation during DJF between an
436 extreme ENSO event ($|\text{SOI}| = 20$) and a neutral phase ($\text{SOI} = 0$). The percentage changes in Figure
437 5 correspond to the posterior median. Red (blue) indicates that extreme El Niño/La Niña increases
438 (decreases) the 1 in 10 year precipitation intensity. During a strong El Niño event, the 1 in 10 year
439 precipitation can increase by 20% to 50% in southern North America and southeast China, about
440 40% in southeast South America, and 10% to 20% in central North America. A decrease of 10%
441 can be observed in western North America and 10% to 20% in northern Southeast Asia.

442

443 During a strong La Niña episode, the 1 in 10 year precipitation increases (relative to neutral
444 conditions) by about 80% in southwest Western Australia, 40% in eastern Australia, 20% in
445 southern Australia and northeast China, 10% in northern Southeast Asia, central North America and
446 northern Europe, and 10% to 40% (from east to west) in South Africa. However, the intensity of the

447 1 in 10 year precipitation decreases in southern North America (about 50% in Mexico) and northern
448 India (about 20%). Further investigation on the 80% increase in southwest Western Australia
449 reveals that DJF is not the main precipitation season, thus the absolute increase in annual maximum
450 precipitation is actually not large. However, a 40% increase in eastern Australia will correspond to
451 much larger absolute increases in extreme precipitation, which may lead to societally important
452 events such as the Queensland flood in 2010-2011 (Cai and van Rensch, 2012).

453 **4.3 Seasonality of the effect of ENSO on extreme precipitations**

454 The results shown in Figure 5 can be further summarized to get an overview of the ENSO effect for
455 all four seasons. This is achieved as follows: the percentage changes shown in Figure 5 for
456 individual stations are summarized as boxplots for each of the 19 areas defined in Figure 1 and for
457 each season. This yields the synthetic representation shown in Figure 6. Note that in this figure,
458 boxplots represent the range of quantile changes from individual gauges within each area. However,
459 the sampling uncertainty in quantile change estimates is ignored in this representation.
460 Consequently, the boxplots should not be interpreted in terms of assessing the statistical
461 significance of quantile changes. However, as a reminder of this sampling variability, we highlight
462 in bold the seasons with moderate or strong ENSO effect as given by Table 2. If the box does not
463 encompass the zero value, it means that ENSO has potential effects over the area, however it still
464 needs to be confirmed through Table 2. Sometimes the box contains the zero value but the effect of
465 ENSO for that season is moderate or strong; this means that significant ENSO effects are only
466 detected in a sub-area rather than the whole area. Table 3 qualitatively summarizes the main areas
467 and seasons affected by ENSO with the consideration of both Table 2 and Figure 6.

468

469 In general, DJF is the season with the strongest ENSO effect, and JJA is the season with the
470 weakest effect for both phases. For the El Niño phase, positive effects are mainly found in central

471 and southern North America, southeast and northeast China, and southeast South America during
472 DJF and surrounding seasons, while negative effects are mainly found in southern and eastern
473 Australia during SON. For the La Niña phase, positive effects are mainly found in western Pacific
474 areas (eastern Asia and Australia) in DJF and surrounding seasons. However, La Niña effects are
475 not very consistent in eastern Pacific areas: positive effects are found in central and western North
476 America in SON, and negative effects are found in southern North America and southeast South
477 America, but in different seasons.

478

479 It is not surprising that the strongest ENSO effects are found in the Pacific areas, especially in the
480 tropical zone. However, to a lesser extent, ENSO also affects northern Europe during DJF for both
481 phases, and the eastern Mediterranean during SON for El Niño. The Indian subcontinent is also
482 affected during the La Niña phase, with the northern and southern parts having different effects in
483 different seasons.

484 **4.4 Asymmetric behavior of ENSO on extreme precipitations**

485 The use of a different linear function in the El Niño and La Niña phases enables the modelling
486 framework to capture and evaluate the asymmetric impact of the ENSO-precipitation relationship.
487 It provides the flexibility to assess at each site whether each ENSO phase can have a positive,
488 negative or no effect on extreme precipitation. If the parameters quantifying the ENSO effect on the
489 location and/or scale parameters are the same in each phase (i.e. $\mu_{reg_1}^- = \mu_{reg_1}^+$ and/or $\sigma_{reg_1}^- = \sigma_{reg_1}^+$),
490 this is a symmetric relationship (often assumed in previous studies) and corresponds to observing
491 opposite effects in the two phases (e.g. precipitation decreases during El Niño but increases during
492 La Niña) (see Figure 7(a)). Conversely, asymmetric behavior corresponds to having non-opposite
493 effects during El Niño and La Niña. The parameters governing the ENSO effect on the location
494 and/or scale parameters are hence different in each phase (i.e. $\mu_{reg_1}^- \neq \mu_{reg_1}^+$ and/or $\sigma_{reg_1}^- \neq \sigma_{reg_1}^+$).

495 There are two ‘types’ of asymmetric behavior: (i) One-phase: no effect for one phase and a strong
496 effect for the other phase. Figure 7(b) shows an example of having strong positive effect during La
497 Niña, but no effect during El Niño. (ii) Two-phase: strong, but non-opposite ENSO effects during
498 both El Niño and La Niña phases. Figure 7(c) shows an example of having strong positive effect
499 during both El Niño and La Niña.

500

501 The last column of Table 3 summarizes the asymmetric nature of the ENSO-extreme precipitation
502 relationship during the season with the strongest effect. In most areas, precipitation is only affected
503 during one phase of ENSO, which corresponds to an asymmetric behavior. Two-phase asymmetric
504 behavior is found in central and western North America, northeast China and northern Europe,
505 where the 10-year precipitation is increased during both strong El Niño and La Niña events (relative
506 to a neutral phase SOI=0). Symmetric behavior is found in southern US during DJF, southern and
507 eastern Australia during SON, and northern Southeast Asia during DJF and SON, where effects of
508 opposite sign are found during two phases.

509 **5 DISCUSSION**

510 **5.1 Practical implications**

511 In the perspective of engineering design and operations, knowledge of how the extreme events
512 change based on ENSO can enable planners to prepare strategies for early response based on ENSO
513 forecast. At a large scale, this information is more important for government officers and policy
514 designers to evaluate in advance the population and potential economic losses associated with the
515 projected flood risk, and to prepare mitigation measures.

516

517 The results of this study have significant practical implications because they provide quantitative
518 estimates of the percentage change in extreme daily precipitation intensity for a unit change in the
519 SOI. Given that ENSO forecasts show some skill at monthly to seasonal lead times (e.g. Jin et al.
520 (2008)), it is possible to use this information to provide quantitative seasonal forecasts of extreme
521 precipitation. From an engineering standpoint, this provides opportunities to improve the
522 management of water resource risks: for instance, dam operation could use the forecasted ENSO
523 state to optimize hydroelectricity production while enforcing appropriate precautionary measures to
524 mitigate flood risk (see e.g. Lima and Lall (2010a)). Another key outcome of this study is the
525 identification of regions with an asymmetric ENSO-precipitation relationship (Table 3 and Figure
526 6). It is possible that current approaches to estimate extreme precipitation quantiles in these regions
527 (which either ignore ENSO or use the symmetric assumption) under-estimate extreme precipitation
528 quantiles. This has practical implications for the design and management of flood-sensitive
529 infrastructure in these regions.

530 **5.2 Changes in ENSO teleconnections**

531 For the more distant future, an important question in terms of ENSO is how the evolution of such an
532 influential global process will affect extreme precipitation in a future climate. Several challenges
533 need to be met to address this issue. Firstly, GCM simulations suggest the possible occurrence of
534 “super-ENSO” events (Latif et al., 2013) in the future, which may require extrapolating from the
535 regional model used in this study well beyond the range of observed SOI values. Whether or not the
536 “piecewise linear” relationship used in this model can be extrapolated to very high SOI values is an
537 open question. Secondly, the ability of GCMs to describe the frequency characteristics (e.g.
538 Johnson et al. (2011)) and the physical mechanisms governing the development of ENSO events
539 remains limited, as discussed, for example, by Bellenger et al. (2013). Note that an interesting
540 potential application of our statistical model would be to apply it to both GCM outputs and

541 observations to assess the ability of GCMs to reproduce the ENSO-extreme precipitation
542 teleconnection and better understand the physical drivers of the asymmetric ENSO-precipitation
543 relationship. This would help evaluate whether projections of future ENSO events can be reliably
544 used to deduce the evolution of extreme precipitation in a future climate.

545 **5.3 Reliability of the definition of a region**

546 An important contribution of this study is the use of a regional statistical model. Indeed, given the
547 available record length and the large local variability of extreme precipitation, a precise
548 quantification of the ENSO effect on extreme precipitation is difficult to achieve without
549 regionalization. The price to pay is the requirement to define homogenous regions. In this study, we
550 defined the regions as grid cells, i.e. according to latitude and longitude only. By repeatedly
551 applying the regional model over geographic regions covering all land areas with available data, the
552 approach has proved a good compromise for the ‘bias-variance’ trade-off. In other words, compared
553 with at-site analysis, the uncertainties are much smaller; compared with global analysis, regional
554 features can still be highlighted.

555

556 It is important to note that for the purposes of the current study only the shape parameter and the
557 ENSO effect parameters are regional. Other parameters are site-specific, which provides the
558 flexibility to account for between-site differences within the region. However, the definition of
559 homogeneous regions adopted in this paper might remain unduly simplistic for some geographical
560 areas. In mountainous areas, in particular, orographic influences can lead to substantial differences
561 in precipitation patterns across small spatial areas. For example, because of the Andes Mountains,
562 precipitation within the grid cells defined across Chile and Argentina may be caused by very
563 different circulation patterns, which are not affected in the same way by ENSO. Thus, assuming the
564 same effect of ENSO in these regions is questionable. A possible solution is to redefine regions by

565 subdividing the grid cells into smaller grids. However, the number of available observation sites
566 might be too low for a meaningful regional analysis. A better outcome might be achieved if the
567 homogeneous regions were based on climate or physiographic variables, or the data characteristics
568 (Bernard et al., 2013; Sun et al., 2015), as opposed to the simple regular grid adopted here.
569 However this requires an understanding of the key driving factors that can lead to precipitation
570 variability in a given area, which are likely to be complex and spatially heterogeneous, and will
571 probably differ depending on the region being analyzed.

572 **5.4 Potential extensions of the statistical model**

573 In addition to improving the definition of regions, several avenues can be identified to extend the
574 statistical model itself. In this discussion, we focus on improving prior specification, using
575 hierarchical models and refining the treatment of spatial dependence.

576 The Bayesian approach has a long history in frequency analysis of both extreme precipitation and
577 floods (e.g. Kuczera, 1999; Vicens et al., 1975; Wood and Rodríguez-Iturbe, 1975a,b). One of its
578 key strengths is the ability to augment the information in the data with additional prior information.
579 For instance, O'Hagan et al. (2006) and Denham and Mengersen (2007) describe general techniques
580 to elicit expert knowledge in the form of a prior distribution, while Viglione et al. (2013) discuss the
581 importance of prior information for flood frequency analysis. In this paper, we used non-
582 informative priors and therefore did not take advantage of this strength of Bayesian estimation. We
583 trialed the use of the general-purpose Martin and Stedinger's prior for the shape parameter (see
584 Section 3.1.4) but it did not bring any noticeable information beyond that already contained in the
585 regional dataset. Further development of appropriate region specific priors by careful investigation
586 of each region's characteristics (e.g. climate and topography) may improve the parameter estimation,
587 in particular for regions with scarce observations.

588 An additional avenue to improve the statistical model is to add some hierarchical component(s) to
589 the model, which can be done naturally in a Bayesian framework. In particular, the current model
590 cannot be used for estimation at ungauged sites due to the existence of local parameters, whose
591 values are site-specific. This could be remedied by using a regression approach to link the values of
592 local parameters with site characteristics such as elevation and distance to sea. A hierarchical
593 modeling approach could then be used to include this regression model, as described by e.g. Cooley
594 et al. (2005) and Renard (2011). Alternatively, the flexibility of the model could be enhanced by
595 allowing ENSO effects to vary in space, but in a smooth way. This can also be achieved with a
596 hierarchical component that would constrain the spatial variations of ENSO effects to follow a
597 chosen spatial hyper-distribution.

598 Finally, the treatment of spatial dependence could also be refined in at least two ways. The first is to
599 refine the dependence-distance relationship of Eq.(4), by moving beyond the Euclidean distance to
600 explain spatial dependence. In particular, orographic effects are likely to play an important role in
601 some regions, and they could be included in the spatial dependence model (see for instance
602 Blanchet and Davison (2011) in the context of a snow depth variable). A second way is to replace
603 the Gaussian copula with another model of spatial dependence. For instance, the Student copula
604 (another member of the Elliptical copula family) could be used to account for asymptotic
605 dependence. Alternative approaches include pair-copula models (Gräler and Pebesma, 2011) or
606 max-stable models (e.g. Westra and Sisson (2011) and Ribatet et al. (2012)). We stress however
607 that the data selection procedure adopted in this paper limits the amount of spatial dependence: the
608 selection of a single site for each of the 16 sub-regions within a region (see section 2.2.2 and Figure
609 2) avoids the selection of many close, highly-dependent pairs of sites. In this context, a Gaussian
610 copula may be sufficient as a first-order approximation to capture the dependence observed in the
611 data. In other contexts (e.g. more highly-dependent pairs of sites, or necessity to extrapolate the

612 dependence structure well beyond observed levels), a finer treatment of spatial dependence may be
613 required.

614 **5.5 Impact of other large scale modes of climate variability**

615 Besides ENSO, other large scale modes of climate variability could also affect regional extreme
616 precipitation. For instance, the Indian Ocean Dipole (IOD) affects the precipitation in northern
617 Southeast Asia and Australia, and the North Atlantic Oscillation influences precipitation in North
618 America and Europe. Research also indicates that in many regions, precipitation is influenced by
619 the combined effect of distinct large scale modes (e.g., Keim and Verdon-Kidd (2009); the IOD and
620 ENSO both influence precipitation in Australia.) However, the ways in which the two modes
621 combine to influence extreme precipitation at the global scale requires further investigation.

622

623 The current study was a purely statistical analysis of the effect of ENSO on extreme precipitation,
624 and does not provide any indication on the physical mechanisms governing such climate-
625 precipitation teleconnections. If such a physical mechanism could be understood, it might lead to a
626 more physically-based regression model structure (rather than the piecewise linear model adopted in
627 this study) to provide a better evaluation of the ENSO effect on extreme precipitation.

628 **6 CONCLUSIONS**

629 We applied a climate-informed regional frequency analysis framework to describe the global
630 pattern of the effect of ENSO on extreme precipitation, focusing particularly on extreme quantiles.
631 The ENSO effects over many regions are quantified along with associated uncertainties. This study
632 goes beyond merely studying the relationship between ENSO and “extreme” precipitation indices,
633 and is extended to more ‘design-relevant’ extreme events (e.g. 1 in 10 year precipitation). The

634 technique of regionalizing the ENSO effects significantly strengthens our ability to quantify such
635 effects.

636

637 Keeping in mind the limitation of the HadEx2 data set (whose uneven spatial sampling favors
638 temperate climates), we draw the following conclusions from the analyses carried out in this
639 paper: (i) ENSO significantly affects extreme precipitation across large parts of the world, which are
640 not limited to Pacific areas; (ii) the ENSO effect varies substantially by season, but DJF is in
641 general the season with the strongest ENSO effect, with the greatest changes, up to 50% higher or
642 lower, in the 1 in 10 year precipitation quantiles between a strong El Niño/La Niña event ($|SOI|=20$)
643 and a neutral phase ($SOI=0$); and (iii) the relationship is asymmetric. In most places, extreme
644 precipitation is significantly influenced during only one phase. Two-phase asymmetry (with strong
645 but non-opposite effects during El Niño and La Niña) is also found in several areas, e.g. central
646 North America and northeast China. In contrast, a symmetric behavior is only found in southern US
647 during DJF, southern and eastern Australia during SON, and northern Southeast Asia during DJF
648 and SON.

649 **7 ACKNOWLEDGEMENTS**

650 We wish to acknowledge Dr Lisa Alexander who provided us with the global observed extreme
651 precipitation HadEx2 dataset. This data set is now available at <http://www.climdex.org/index.html>.

652 We wish to acknowledge Prof. Dmitri Kavetski for providing the FORTRAN library DMSL.
653 Rfortran software library (Thyer et al., 2011) is used for the data and commands transfer between
654 FORTRAN and R. Dr Westra's time was supported by Australian Research Council (ARC)
655 Discovery project DP150100411. We also wish to acknowledge the research funding provided by
656 Electricité de France (EDF), Irstea DRI, Région Rhône-Alpes (Explora'doc), the University of Adelaide
657 (through ARC Discovery Project DP1094796) and the American International Group (CU12-2326).

659 **8 REFERENCES**

- 660 Ahern, M., Kovats, R.S., Wilkinson, P., Few, R., Matthies, F., 2005. Global health impacts of floods: Epidemiologic
661 evidence. *Epidemiologic Reviews*, 27: 36-46.
- 662 Alexander, L.V., Uotila, P., Nicholls, N., 2009. Influence of sea surface temperature variability on global temperature
663 and precipitation extremes. *Journal of Geophysical Research-Atmospheres*, 114. DOI:10.1029/2009jd012301
- 664 Aryal, S.K. et al., 2009. Characterizing and modeling temporal and spatial trends in rainfall extremes. *Journal of*
665 *Hydrometeorology*, 10(1): 241-253.
- 666 Bellenger, H., Guilyardi, E., Leloup, J., Lengaigne, M., Vialard, J., 2013. ENSO representation in climate models: from
667 CMIP3 to CMIP5. *Climate Dynamics*: 1-20. DOI:10.1007/s00382-013-1783-z
- 668 Benjamini, Y., Hochberg, Y., 1995. Controlling the False Discovery Rate: A Practical and Powerful Approach to
669 Multiple Testing. *Journal of the Royal Statistical Society. Series B (Methodological)*, 57(1): 289-300.
670 DOI:10.2307/2346101
- 671 Bernard, E., Naveau, P., Vrac, M., Mestre, O., 2013. Clustering of maxima: Spatial dependencies among heavy rainfall
672 in France. *Journal of Climate*, 26(20): 7929-7937.
- 673 Blanchet, J., Davison, A.C., 2011. Spatial Modeling of Extreme Snow Depth. *Ann Appl Stat*, 5(3): 1699-1725. DOI:Doi
674 10.1214/11-Aoas464
- 675 Cai, W., Cowan, T., 2009. La Nina Modoki impacts Australia autumn rainfall variability. *Geophysical Research Letters*,
676 36. DOI:Artn L12805
677 Doi 10.1029/2009gl037885
- 678 Cai, W., van Rensch, P., 2012. The 2011 southeast Queensland extreme summer rainfall: A confirmation of a negative
679 Pacific Decadal Oscillation phase? *Geophys Res Lett*, 39. DOI:10.1029/2011gl050820
- 680 Cai, W., van Rensch, P., Cowan, T., Sullivan, A., 2010. Asymmetry in ENSO teleconnection with regional rainfall, its
681 multidecadal variability, and impact. *Journal of Climate*, 23(18): 4944-4955. DOI:10.1175/2010jcli3501.1
- 682 Castello, A.F., Shelton, M.L., 2004. Winter precipitation on the US Pacific Coast and El Nino Southern oscillation
683 events. *International Journal of Climatology*, 24(4): 481-497. DOI:10.1002/joc.1011
- 684 Cayan, D.R., Redmond, K.T., Riddle, L.G., 1999. ENSO and hydrologic extremes in the western United States. *Journal*
685 *of Climate*, 12(9): 2881-2893. DOI:10.1175/1520-0442(1999)012<2881:eaheit>2.0.co;2
- 686 Chen, J.M., Li, T., Shih, C.F., 2008. Asymmetry of the El Nino-spring rainfall relationship in Taiwan. *J. Meteorol. Soc.*
687 *Jpn.*, 86(2): 297-312. DOI:10.2151/jmsj.86.297
- 688 Coles, S., 2001. An introduction to statistical modeling of extreme values, 208. Springer, London.
- 689 Coles, S., Pericchi, L.R., Sisson, S., 2003. A fully probabilistic approach to extreme rainfall modeling. *Journal of*
690 *Hydrology*, 273(1-4): 35 - 50.
- 691 Cooley, D., Nychka, D., Naveau, P., 2005. A spatial Bayesian hierarchical model for a precipitation return levels map.
692 *Extreme value analysis*, Gothenburg, Sweden.
- 693 Curtis, S. et al., 2007. Precipitation extremes estimated by GPCP and TRMM: ENSO relationships. *Journal of*
694 *Hydrometeorology*, 8(4): 678-689. DOI:10.1175/jhm601.1
- 695 Dai, A., Fung, I.Y., DelGenio, A.D., 1997. Surface observed global land precipitation variations during 1900-88.
696 *Journal of Climate*, 10(11): 2943-2962. DOI:Doi 10.1175/1520-0442(1997)010<2943:Soglpv>2.0.Co;2
- 697 Dai, A., Wigley, T.M.L., 2000. Global patterns of ENSO-induced precipitation. *Geophys Res Lett*, 27(9): 1283-1286.
698 DOI:Doi 10.1029/1999gl011140
- 699 Denham, R., Mengersen, K., 2007. Geographically assisted elicitation of expert opinion for regression models.
700 *Bayesian Analysis*, 2(1): 99-135.
- 701 Donat, M.G. et al., 2013. Updated analyses of temperature and precipitation extreme indices since the beginning of the
702 twentieth century: The HadEX2 dataset. *Journal of Geophysical Research: Atmospheres*, 118(5): 2098-2118.
703 DOI:10.1002/jgrd.50150
- 704 Favre, A.C., El Adlouni, S., Perreault, L., Thiemonge, N., Bobee, B., 2004. Multivariate hydrological frequency
705 analysis using copulas. *Water Resources Research*, 40(1): W01101.
- 706 Feng, J., Li, J.P., 2011. Influence of El Nino Modoki on spring rainfall over south China. *Journal of Geophysical*
707 *Research-Atmospheres*, 116. DOI:Artn D13102
708 Doi 10.1029/2010jd015160
- 709 Fernandez, H.W., Fernandez, B., 2002. The influence of ENSO in the precipitation regime in southern South America.
710 *Ingenieria Hidraulica En Mexico*, 17(3): 5-16.
- 711 Fisher, R.A., Tippett, L.H.C., 1928. Limiting forms of the frequency distribution of the largest or smallest member of a
712 sample. *Mathematical Proceedings of the Cambridge Philosophical Society*, 24(02): 180-190.

- 713 Frey, H.C., Burmaster, D.E., 1999. Methods for characterizing variability and uncertainty: comparison of bootstrap
714 simulation and likelihood-based approaches. *Risk Analysis*, 19(1): 109-130.
- 715 Gelman, A., Rubin, D.B., 1992. Inference from iterative simulation using multiple sequences. *Statistical science*, 7:
716 457-472.
- 717 Gershunov, A., Barnett, T.P., 1998. ENSO influence on intraseasonal extreme rainfall and temperature frequencies in
718 the contiguous United States: Observations and model results. *Journal of Climate*, 11(7): 1575-1586.
719 DOI:10.1175/1520-0442(1998)011<1575:eioier>2.0.co;2
- 720 Gräler, B., Pebesma, E., 2011. The pair-copula construction for spatial data: a new approach to model spatial
721 dependency. *Procedia Environmental Sciences*, 7: 206-211.
- 722 Grimm, A.M., 2011. Interannual climate variability in South America: impacts on seasonal precipitation, extreme
723 events, and possible effects of climate change. *Stochastic Environmental Research and Risk Assessment*,
724 25(4): 537-554. DOI:10.1007/s00477-010-0420-1
- 725 Grimm, A.M., Tedeschi, R.G., 2009. ENSO and extreme rainfall events in South America. *Journal of Climate*, 22(7):
726 1589-1609. DOI:10.1175/2008jcli2429.1
- 727 Hanel, M., Buishand, T.A., Ferro, C.A.T., 2009. A nonstationary index flood model for precipitation extremes in
728 transient regional climate model simulations. *Journal of Geophysical Research-Atmospheres*, 114. DOI:Artn
729 D15107
730 Doi 10.1029/2009jd011712
- 731 Hannachi, A., 2001. Toward a nonlinear identification of the atmospheric response to ENSO. *Journal of Climate*, 14(9):
732 2138-2149. DOI:10.1175/1520-0442(2001)014<2138:taniot>2.0.co;2
- 733 Higgins, R.W., Kousky, V.E., Xie, P., 2011. Extreme precipitation events in the south-central United States during May
734 and June 2010: Historical perspective, role of ENSO, and trends. *Journal of Hydrometeorology*, 12(5): 1056-
735 1070. DOI:10.1175/jhm-d-10-05039.1
- 736 Hoerling, M.P., Kumar, A., Xu, T.Y., 2001. Robustness of the nonlinear climate response to ENSO's extreme phases.
737 *Journal of Climate*, 14(6): 1277-1293. DOI:10.1175/1520-0442(2001)014<1277:rotncr>2.0.co;2
- 738 Hoerling, M.P., Kumar, A., Zhong, M., 1997. El Nino, La Nina, and the nonlinearity of their teleconnections. *Journal of*
739 *Climate*, 10(8): 1769-1786. DOI:10.1175/1520-0442(1997)010<1769:enolna>2.0.co;2
- 740 Jin, E. et al., 2008. Current status of ENSO prediction skill in coupled ocean-atmosphere models. *Climate Dynamics*,
741 31(6): 647-664. DOI:10.1007/s00382-008-0397-3
- 742 Johnson, F., Westra, S., Sharma, A., Pitman, A.J., 2011. An assessment of GCM skill in simulating persistence across
743 multiple time scales. *Journal of Climate*, 24(14): 3609-3623. DOI:10.1175/2011JCLI3732.1
- 744 Jones, C., Carvalho, L.M.V., 2012. Spatial-intensity variations in extreme precipitation in the Contiguous United States
745 and the Madden-Julian Oscillation. *Journal of Climate*, 25(14): 4898-4913. DOI:10.1175/jcli-d-11-00278.1
- 746 Kane, R.P., 1999. El Nino timings and rainfall extremes in India, Southeast Asia and China. *International Journal of*
747 *Climatology*, 19(6): 653-672. DOI:10.1002/(sici)1097-0088(199905)19:6<653::aid-joc379>3.3.co;2-3
- 748 Katz, R.W., Parlange, M.B., Naveau, P., 2002. Statistics of extremes in hydrology. *Advances in Water Resources*, 25(8-
749 12): 1287 - 1304.
- 750 Kayano, M.T., Andreoli, R.V., 2006. Relationships between rainfall anomalies over northeastern Brazil and the El
751 Nino-Southern Oscillation. *Journal of Geophysical Research-Atmospheres*, 111(D13).
752 DOI:10.1029/2005jd006142
- 753 Keim, A.S., Verdon-Kidd, D.C., 2009. Climatic drivers of Victorian streamflow: Is ENSO the dominant influence?
754 *Australian Journal of Water Resources*, 13(1): 17.
- 755 Kenyon, J., Hegerl, G.C., 2010. Influence of modes of climate variability on global precipitation extremes. *Journal of*
756 *Climate*, 23(23): 6248-6262. DOI:10.1175/2010jcli3617.1
- 757 King, A.D., Alexander, L.V., Donat, M.G., 2013. Asymmetry in the response of eastern Australia extreme rainfall to
758 low-frequency Pacific variability. *Geophys Res Lett*: 1-6. DOI:10.1002/grl.50427
- 759 Kripalani, R.H., Kulkarni, A., 1997. Rainfall variability over South-east Asia - Connections with Indian monsoon and
760 enso extremes: New perspectives. *International Journal of Climatology*, 17(11): 1155-1168.
761 DOI:10.1002/(sici)1097-0088(199709)17:11<1155::aid-joc188>3.0.co;2-b
- 762 Kruger, A.C., 1999. The influence of the decadal-scale variability of summer rainfall on the impact of El Nino and La
763 Nina events in South Africa. *International Journal of Climatology*, 19(1): 59-68. DOI:10.1002/(sici)1097-
764 0088(199901)19:1<59::aid-joc347>3.3.co;2-2
- 765 Kuczera, G., 1999. Comprehensive at - site flood frequency analysis using Monte Carlo Bayesian inference. *Water*
766 *Resources Research*, 35(5): 1551-1557.
- 767 Kwon, H.-H., Khalil, A.F., Siegfried, T., 2008. Analysis of extreme summer rainfall using climate teleconnections and
768 typhoon characteristics in South Korea. *J Am Water Resour As*, 44(2): 436-448. DOI:10.1111/j.1752-
769 1688.2008.00173.x
- 770 Latif, M., Semenov, V., Wonsun, P., 2013. Super El Niños in a Warming World, EGU General Assembly Conference
771 Abstracts, pp. 5348.

- 772 Li, C., Ma, H., 2012. Relationship between ENSO and winter rainfall over Southeast China and its decadal variability.
773 *Adv Atmos Sci*, 29(6): 1129-1141. DOI:DOI 10.1007/s00376-012-1248-z
- 774 Lima, C.H.R., Lall, U., 2010a. Climate informed long term seasonal forecasts of hydroenergy inflow for the Brazilian
775 hydropower system. *Journal of Hydrology*, 381(1–2): 65-75.
776 DOI:<http://dx.doi.org/10.1016/j.jhydrol.2009.11.026>
- 777 Lima, C.H.R., Lall, U., 2010b. Spatial scaling in a changing climate: A hierarchical bayesian model for non-stationary
778 multi-site annual maximum and monthly streamflow. *Journal of Hydrology*, 383(3-4): 307-318.
- 779 Lyon, B., Barnston, A.G., 2005. ENSO and the spatial extent of interannual precipitation extremes in tropical land
780 areas. *Journal of Climate*, 18(23): 5095-5109. DOI:10.1175/jcli3598.1
- 781 Mannshardt-Shamseldin, E.C., Smith, R.L., Sain, S.R., Mearns, L.O., Cooley, D., 2010. Downscaling extremes: A
782 comparison of extreme value distributions in point-source and gridded precipitation data. *The Annals of*
783 *Applied Statistics*: 484-502.
- 784 Martins, E.S., Stedinger, J.R., 2000. Generalized maximum-likelihood generalized extreme-value quantile estimators
785 for hydrologic data. *Water Resources Research*, 36(3): 737-744. DOI:10.1029/1999WR900330
- 786 Meehl, G.A., Tebaldi, C., Teng, H., Peterson, T.C., 2007. Current and future US weather extremes and El Nino.
787 *Geophys Res Lett*, 34(20). DOI:10.1029/2007gl031027
- 788 Min, S.K., Cai, W.J., Whetton, P., 2013. Influence of climate variability on seasonal extremes over Australia. *Journal of*
789 *Geophysical Research-Atmospheres*, 118(2): 643-654. DOI:10.1002/jgrd.50164
- 790 O'Hagan, A. et al., 2006. *Uncertain judgements: eliciting experts' probabilities*. John Wiley & Sons.
- 791 OrtizBevia, M.J., Perez-Gonzalez, I., Alvarez-Garcia, F.J., Gershunov, A., 2010. Nonlinear estimation of El Nino
792 impact on the North Atlantic winter. *Journal of Geophysical Research-Atmospheres*, 115.
793 DOI:10.1029/2009jd013387
- 794 Ouarda, T.B.M.J., El-Adlouni, S., 2011. Bayesian nonstationary frequency analysis of hydrological variables. *J Am*
795 *Water Resour As*, 47(3): 496-505. DOI:DOI 10.1111/j.1752-1688.2011.00544.x
- 796 Pscheidt, I., Grimm, A.M., 2009. Frequency of extreme rainfall events in Southern Brazil modulated by interannual and
797 interdecadal variability. *International Journal of Climatology*, 29(13): 1988-2011. DOI:10.1002/joc.1799
- 798 Renard, B., 2011. A Bayesian hierarchical approach to regional frequency analysis. *Water Resources Research*, 47(11):
799 W11513. DOI:10.1029/2010WR010089
- 800 Renard, B., Garreta, V., Lang, M., 2006a. An application of Bayesian analysis and Markov chain Monte Carlo methods
801 to the estimation of a regional trend in annual maxima. *Water Resources Research*, 42(12): W12422.
- 802 Renard, B., Lang, M., 2007. Use of a Gaussian copula for multivariate extreme value analysis: Some case studies in
803 hydrology. *Advances in Water Resources*, 30(4): 897-912.
- 804 Renard, B., Lang, M., Bois, P., 2006b. Statistical analysis of extreme events in a non-stationary context via a Bayesian
805 framework: case study with peak-over-threshold data. *Stochastic Environmental Research and Risk*
806 *Assessment*, 21(2): 97-112. DOI:DOI 10.1007/s00477-006-0047-4
- 807 Renard, B. et al., 2008. Regional methods for trend detection: Assessing field significance and regional consistency.
808 *Water Resources Research*, 44(8). DOI:Artn W08419
809 Doi 10.1029/2007wr006268
- 810 Renard, B., Sun, X., Lang, M., 2013. Bayesian methods for non-stationary extreme value analysis. In: AghaKouchak,
811 A., Easterling, D., Hsu, K., Schubert, S., Sorooshian, S. (Eds.), *Extremes in a changing climate: Detection,*
812 *analysis and uncertainty*. Water Science and Technology Library. Springer Netherlands, pp. 39-95.
813 DOI:10.1007/978-94-007-4479-0_3
- 814 Ribatet, M., Cooley, D., Davison, A.C., 2012. Bayesian inference from composite likelihoods, with an application to
815 spatial extremes. *Stat. Sin.*, 22(2): 813-845.
- 816 Ropelewski, C.F., Halpert, M.S., 1987. Global and regional scale precipitation patterns associated with the El-Nino
817 Southern Oscillation. *Mon Weather Rev.*, 115(8): 1606-1626. DOI:Doi 10.1175/1520-
818 0493(1987)115<1606:Garspp>2.0.Co;2
- 819 Sardeshmukh, P.D., Compo, G.P., Penland, C., 2000. Changes of probability associated with El Nino. *Journal of*
820 *Climate*, 13(24): 4268-4286. DOI:10.1175/1520-0442(2000)013<4268:copawe>2.0.co;2
- 821 Schubert, S.D., Chang, Y., Suarez, M.J., Pegion, P.J., 2008. ENSO and wintertime extreme precipitation events over the
822 contiguous united states. *Journal of Climate*, 21(1): 22-39. DOI:10.1175/2007jcli1705.1
- 823 Shang, H., Yan, J., Zhang, X., 2011. El Nino-Southern Oscillation influence on winter maximum daily precipitation in
824 California in a spatial model. *Water Resources Research*, 47. DOI:10.1029/2011wr010415
- 825 Sun, X., Lall, U., Merz, B., Dung, N.V., 2015. Hierarchical Bayesian clustering for nonstationary flood frequency
826 analysis: Application to trends of annual maximum flow in Germany. *Water Resources Research*: (in press).
827 <http://dx.doi.org/10.1002/2015WR017117>. DOI:10.1002/2015WR017117
- 828 Sun, X., Thyer, M., Renard, B., Lang, M., 2014. A general regional frequency analysis framework for quantifying local-
829 scale climate effects: A case study of ENSO effects on Southeast Queensland rainfall. *Journal of Hydrology*,
830 512(0): 53-68. DOI:<http://dx.doi.org/10.1016/j.jhydrol.2014.02.025>

- 831 Thyer, M., Leonard, M., Kavetski, D., Need, S., Renard, B., 2011. The open source RFortran library for accessing R
832 from Fortran, with applications in environmental modelling. *Environ Modell Softw*, 26(2): 219-234. DOI:DOI
833 10.1016/j.envsoft.2010.05.007
- 834 Tramblay, Y. et al., 2012. Climate change impacts on extreme precipitation in Morocco. *Global and Planetary Change*,
835 82-83: 104-114. DOI:10.1016/j.gloplacha.2011.12.002
- 836 Vanheerden, J., Terblanche, D.E., Schulze, G.C., 1988. The Southern Oscillation and South-African Summer Rainfall. *J*
837 *Climatol*, 8(6): 577-597.
- 838 Ventura, V., Paciorek, C.J., Risbey, J.S., 2004. Controlling the Proportion of Falsely Rejected Hypotheses when
839 Conducting Multiple Tests with Climatological Data. *Journal of Climate*, 17(22): 4343-4356.
840 DOI:10.1175/3199.1
- 841 Vicens, G.J., Rodriguez - Iturbe, I., Schaake, J.C., 1975. A Bayesian framework for the use of regional information in
842 hydrology. *Water Resources Research*, 11(3): 405-414.
- 843 Viglione, A., Merz, R., Salinas, J.L., Blöschl, G., 2013. Flood frequency hydrology: 3. A Bayesian analysis. *Water*
844 *Resources Research*, 49(2): 675-692.
- 845 Wan, S.Q., Hu, Y.L., You, Z.Y., Kang, J.P., Zhu, J.G., 2013. Extreme monthly precipitation pattern in China and its
846 dependence on Southern Oscillation. *International Journal of Climatology*, 33(4): 806-814.
847 DOI:10.1002/joc.3466
- 848 Ward, P.J., Eisner, S., Flörke, M., Dettinger, M.D., Kummerow, M., 2014a. Annual flood sensitivities to El Niño–Southern
849 Oscillation at the global scale. *Hydrology and Earth System Sciences*, 18(1): 47-66.
- 850 Ward, P.J. et al., 2014b. Strong influence of El Niño Southern Oscillation on flood risk around the world. *Proceedings*
851 *of the National Academy of Sciences*, 111(44): 15659-15664. DOI:10.1073/pnas.1409822111
- 852 Westra, S. et al., 2014. Future changes to the intensity and frequency of short-duration extreme rainfall. *Reviews of*
853 *Geophysics*, 52(3): 2014RG000464. DOI:10.1002/2014RG000464
- 854 Westra, S., Sisson, S.A., 2011. Detection of non-stationarity in precipitation extremes using a max-stable process
855 model. *Journal of Hydrology*, 406(1-2): 119-128. DOI:DOI 10.1016/j.jhydrol.2011.06.014
- 856 Wood, E.F., Rodríguez-Iturbe, I., 1975a. A Bayesian approach to analyzing uncertainty among flood frequency models.
857 *Water Resources Research*, 11(6): 839-843. DOI:10.1029/WR011i006p00839
- 858 Wood, E.F., Rodríguez-Iturbe, I., 1975b. Bayesian inference and decision making for extreme hydrologic events. *Water*
859 *Resources Research*, 11(4): 533-542. DOI:10.1029/WR011i004p00533
- 860 Wu, A.M., Hsieh, W.W., Shabbar, A., 2005. The nonlinear patterns of North American winter temperature and
861 precipitation associated with ENSO. *Journal of Climate*, 18(11): 1736-1752. DOI:10.1175/jcli3372.1
- 862 Wu, R.G., Hu, Z.Z., Kirtman, B.P., 2003. Evolution of ENSO-related rainfall anomalies in East Asia. *Journal of*
863 *Climate*, 16(22): 3742-3758. DOI:Doi 10.1175/1520-0442(2003)016<3742:Eoerai>2.0.Co;2

864

865

866 List of captions

867 Tables

868 TABLE 1: SUMMARY OF GOODNESS-OF-FIT FOR ALL REGIONS. “#” MEANS “NUMBER OF”.

869 TABLE 2: QUALITATIVE SUMMARY OF THE EFFECTS OF ENSO ON THE LOCATION AND SCALE PARAMETERS. ARROWS DENOTE AREAS WITH
 870 REMARKABLE EFFECT OF ENSO WHERE A SIGNIFICANT EFFECT IS FOUND IN MANY CONTINUOUS REGIONS WITHIN THE AREA. ‘↓’ DENOTES
 871 A NEGATIVE EFFECT AND ‘↑’ DENOTES A POSITIVE EFFECT ON THE LOCATION PARAMETER. SINGLE ARROW DESCRIBES A MODERATE
 872 EFFECT, WHILE DOUBLE ARROW DESCRIBES A STRONG EFFECT FOR THE ABSOLUTE SLOPE VALUE LARGER THAN 0.2. THE UNDERLINED
 873 ARROWS DESCRIBE THAT SAME EFFECT OF ENSO IS ALSO DETECTED ON THE SCALE PARAMETER.

874 TABLE 3: QUALITATIVE SUMMARY OF THE EFFECT OF ENSO ON QUANTILES. “↑” DENOTES THE SEASONS IN WHICH EL NIÑO/LA NIÑA HAS A
 875 POSITIVE EFFECT, WHILE “↓” DENOTES A NEGATIVE EFFECT. THE SEASONS ARE SORTED IN DESCENDING ORDER ACCORDING TO STRENGTH
 876 OF THE EFFECT OF ENSO. IF THE EFFECT THE ENSO IS NOT STRONG OVER THE WHOLE AREA, SUB-AREA WITH STRONG EFFECT IS
 877 SPECIFIED IN THE PARENTHESES.

878 Figures

879 FIGURE 1: LOCATION OF HIGH QUALITY OBSERVATION SITES WITH MORE THAN 40 YEARS OF RECORD (RED DOTS) FROM HADEX2 DATASET.
 880 RESULTS OF THIS STUDY WILL BE SUMMARIZED FOR THE NINETEEN AREAS REPRESENTED BY BLACK BOXES.

881 FIGURE 2: SCHEMATIC OF OBSERVATION SITE SELECTION FOR EACH GRID CELL.

882 FIGURE 3: SLOPE OF THE LOCATION PARAMETER WITH RESPECT TO SOI DURING EL NIÑO ($\mu_{reg_1}^-$) AND LA NIÑA ($\mu_{reg_1}^+$) PHASES FOR DJF
 883 SEASON. SMALL GREY DOTS DENOTE CELLS WITH TOO FEW DATA STATIONS TO PERFORM A REGIONAL ANALYSIS. DOTS WITH RED (BLUE)
 884 OUTLINES DENOTE SIGNIFICANTLY POSITIVE (NEGATIVE) SLOPES, WHILE DOTS WITH GREY OUTLINES DENOTE NON-SIGNIFICANT SLOPES.
 885 DOTS WITH YELLOW OUTLINES DENOTE THE DRY REGIONS WITH FREQUENT ZERO PRECIPITATION DURING DJF.

886 FIGURE 4: SAME AS FIGURE 3, BUT FOR SCALE PARAMETERS $\sigma_{reg_1}^-$ (EL NIÑO) AND $\sigma_{reg_1}^+$ (LA NIÑA).

887 FIGURE 5: PERCENTAGE CHANGE FOR THE INTENSITY OF 1 IN 10 YEAR PRECIPITATION RELATIVE TO SOI=0 FOR INDIVIDUAL GAUGE LOCATIONS
 888 FOR DJF SEASON. GREY DOTS DENOTE CELLS WITH TOO LITTLE STATION DATA TO PERFORM A REGIONAL ANALYSIS. RED (BLUE) DOTS
 889 DENOTE AN INCREASE (DECREASE) IN THE INTENSITY OF A 1 IN 10 YEAR PRECIPITATION EVENT FOR STRONG EL NIÑO/LA NIÑA PHASES
 890 COMPARED WITH A NEUTRAL PHASE. YELLOW DOTS DENOTE THE DRY REGIONS WITH FREQUENT ZERO PRECIPITATIONS DURING DJF.

891 FIGURE 6: THE EFFECT OF EL NIÑO AND LA NIÑA ON THE 1 IN 10 YEAR PRECIPITATIONS FOR DIFFERENT SEASONS. SAMPLES FOR THE BOXPLOT
892 ARE THE PERCENTAGE CHANGE MEDIAN OF THE PRECIPITATION CALCULATED AT EACH STATION WITHIN THE AREAS SHOWN IN FIGURE 1.
893 THE SEASON WITH MODERATE OR STRONG EFFECT OF ENSO AS GIVEN BY TABLE 2 IS HIGHLIGHTED IN BOLD. (A HIGH RESOLUTION
894 FIGURE IS AVAILABLE ONLINE).

895 FIGURE 7: CONCEPTUAL DIAGRAM OF THE TYPES OF SYMMETRY/ASYMMETRY IN THE RELATIONSHIP BETWEEN ENSO AND EXTREME
896 PRECIPITATION. (A) SYMMETRIC RELATIONSHIP: OPPOSITE EFFECTS IN THE TWO PHASES; (B) ONE PHASE ASYMMETRIC RELATIONSHIP: NO
897 EFFECT FOR ONE PHASE AND A STRONG EFFECT FOR THE OTHER PHASE; (C) TWO PHASE ASYMMETRIC RELATIONSHIP: STRONG, BUT NON-
898 OPPOSITE ENSO EFFECT DURING BOTH THE EL NIÑO AND LA NIÑA PHASES.

899 Supplement

900 S 1: (A) GOODNESS-OF-FIT PP-PLOT OF ALL SIXTEEN STATIONS. (B) DEPENDENCE-DISTANCE RELATIONSHIP OF THE GAUSSIAN TRANSFORMED
901 DATA. THE BLACK DOTS ARE THE EMPIRICAL PAIRWISE CORRELATIONS AND RED LINES ARE THE ESTIMATION FROM THE EXPONENTIAL
902 MODEL (EQ.(4)) WITH 90% CREDIBILITY INTERVAL.

903 S 2: POSTERIOR DISTRIBUTION OF THE REGIONAL PARAMETERS $\mu_{reg_1}^-$, $\mu_{reg_1}^+$ AND ξ . THE FIRST SIXTEEN BOXES ARE THE ESTIMATION WITH
904 NON-INFORMATIVE PRIORS USING FROM ONE TO SIXTEEN STATIONS. THE LAST BOX IS THE ESTIMATION USING ALL SIXTEEN STATIONS
905 WITH MARTINS AND STEDINGER' (MS) GAMMA(6,9) PRIOR FOR THE SHAPE PARAMETER.

906 S 3: SCATTERPLOT OF THE PROBABILITY OF A STATION PAIR EXCEEDING THE 75TH PERCENTILE OF THE AT-SITE HISTORICAL SEASONAL MAXIMUM
907 DAILY PRECIPITATION AMONG THE STATIONS IN A REGION. (A) EMPIRICAL PROBABILITY VS. THEORETICAL PROBABILITY CALCULATED BY
908 THE GAUSSIAN COPULA MODEL; (B) EMPIRICAL PROBABILITY VS. THEORETICAL PROBABILITY CALCULATED BY THE MODEL IGNORING
909 SPATIAL DEPENDENCE. THE DASHED RED LINE IS THE FIT OF A CUBIC SMOOTHING SPLINE.

910

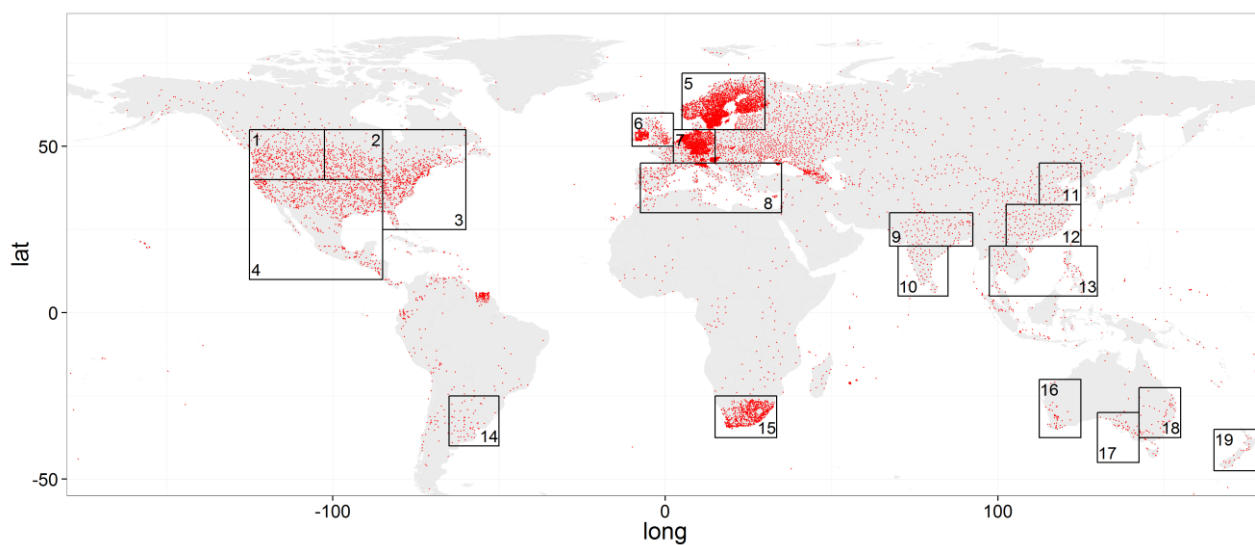
911

912 **Table 1: Summary of goodness-of-fit for all regions. “#” means “number of”.**

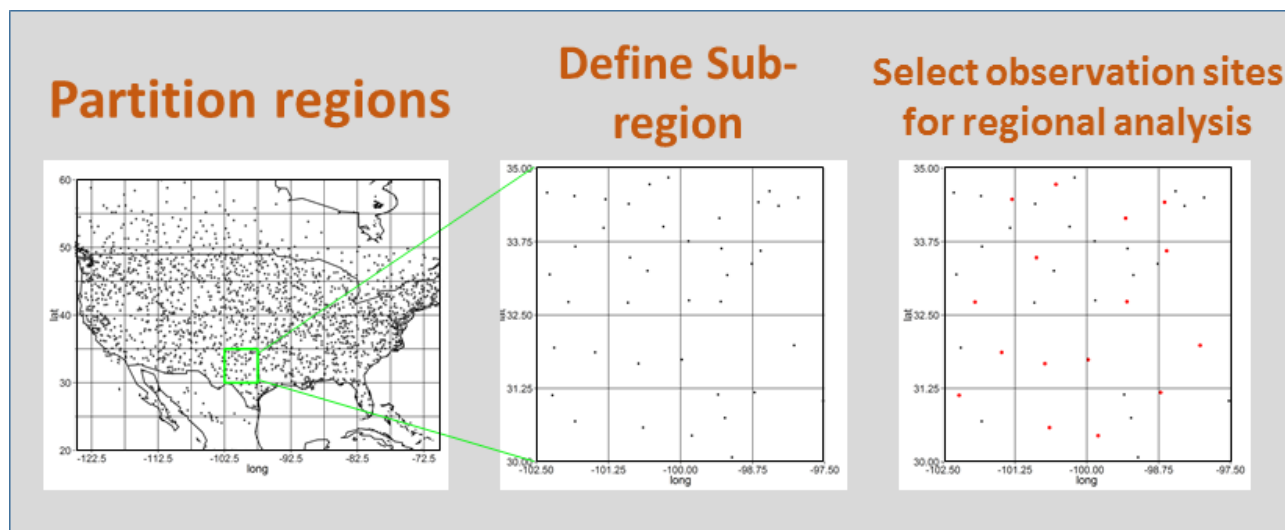
| Season | # regions meeting data requirements | # regions with mostly zero values for seasonal maximum precipitation | # regions where goodness of fit is good | # regions where goodness of fit is poor |
|--------|-------------------------------------|--|---|---|
| DJF | 323 | 12 | 309 | 2 |
| MAM | 323 | 13 | 309 | 1 |
| JJA | 323 | 21 | 301 | 1 |
| SON | 323 | 4 | 319 | 0 |

Table 3: Qualitative summary of the effect of ENSO on quantiles. “↑” denotes the seasons in which El Niño/La Niña has a positive effect, while “↓” denotes a negative effect. The seasons are sorted in descending order according to strength of the effect of ENSO. If the effect the ENSO is not strong over the whole area, sub-area with strong effect is specified in the parentheses.

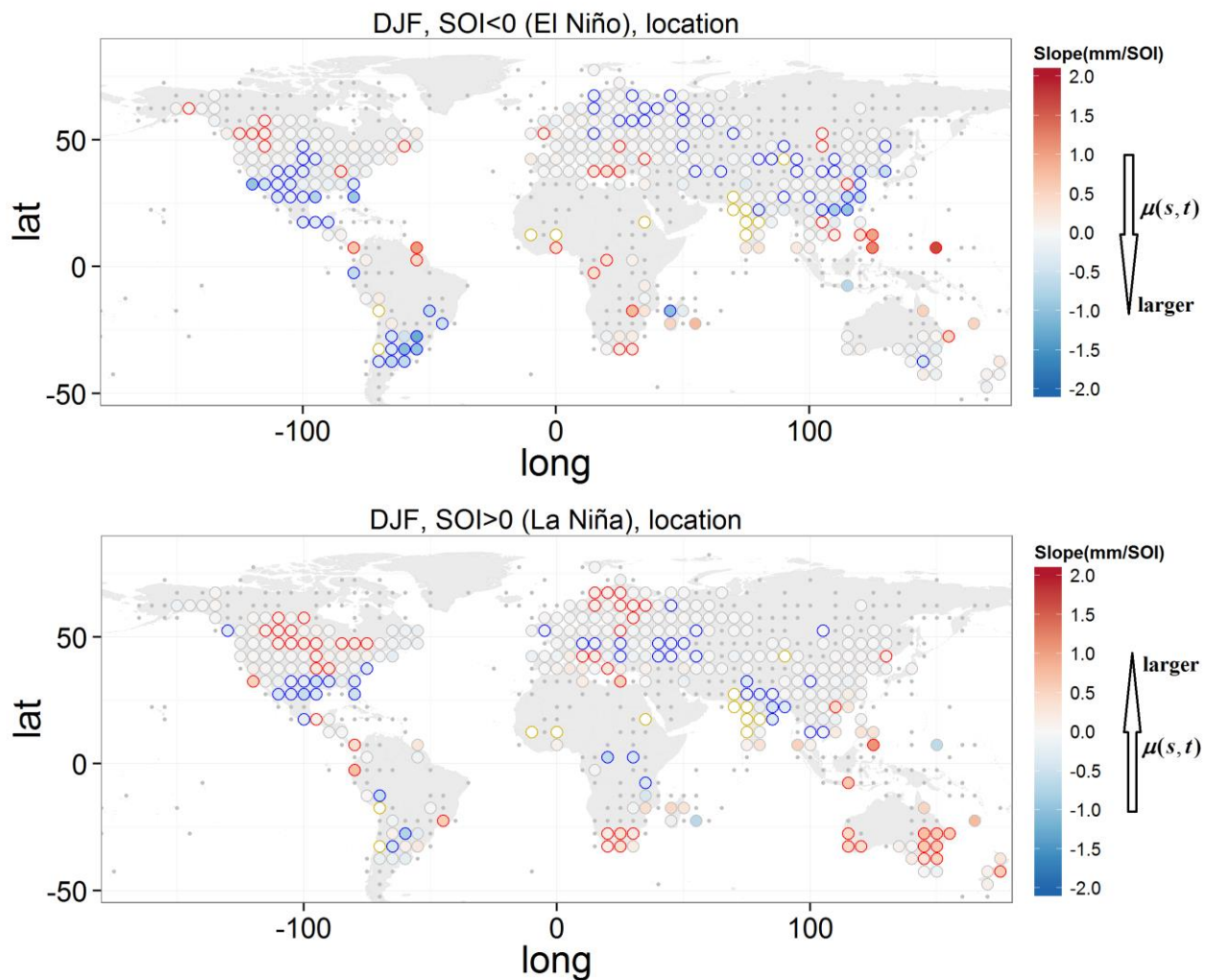
| | Group | Area | El Niño | La Niña | Asymmetry |
|------------------------|-------|------------------------------|---------------------|------------------------|---|
| Most affected regions | I | Central North America | ↑SON,DJF | ↑SON,DJF | Asymmetric, 2 phases |
| | | Southern North America | ↑DJF | ↓MAM,DJF (southern US) | Symmetric |
| | III | Northeast China | ↑DJF,MAM | ↑DJF,MAM | Asymmetric, 2 phases |
| | | Southeast China | ↑DJF | / | Asymmetric, 1 phase |
| | | Northern Southeast Asia | ↓DJF,SON | ↑DJF,MAM,SON, ↓ JJA | Symmetric |
| | IV | Southeast South America | ↑DJF,MAM | ↓SON | Asymmetric, 1 phase |
| | | South Africa | / | ↑DJF,MAM | Asymmetric, 1 phase |
| | | Southwest Western Australia | / | ↑DJF,MAM | Asymmetric, 1 phase |
| | | Southern Australia | ↓SON,JJA | ↑MAM,JJA,SON | Asymmetric, 1 phase (MAM); Symmetric (SON,JJA) |
| | | Eastern Australia | ↓JJA, SON | ↑DJF,SON | Asymmetric, 1 phase (DJF, JJA); Symmetric (SON) |
| Other affected regions | I | Western North America | ↑SON,MAM ↓ DJF | ↑SON | Asymmetric, 2 phases |
| | II | Northern Europe | ↑DJF | ↑DJF | Asymmetric, 2 phases |
| | | Mediterranean | ↑SON (eastern part) | / | Asymmetric, 1 phase |
| | III | Northern Indian subcontinent | / | ↑SON,MAM, ↓ DJF | Asymmetric, 1 phase |
| | | Southern Indian subcontinent | / | ↑JJA | Asymmetric, 1 phase |



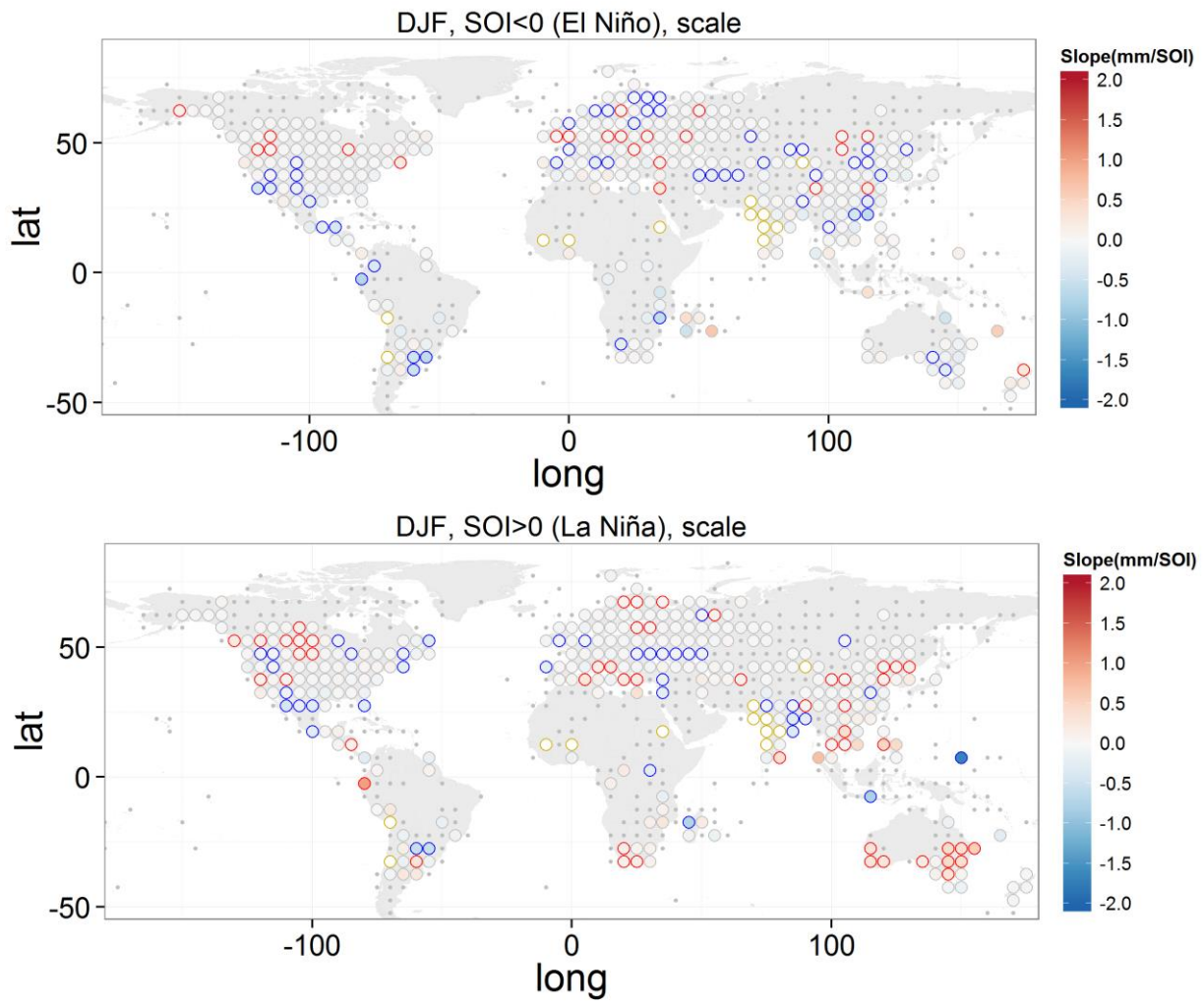
913 **Figure 1: Location of high quality observation sites with more than 40 years of record (red**
914 **dots) from HadEX2 dataset. Results of this study will be summarized for the nineteen areas**
915 **represented by black boxes.**



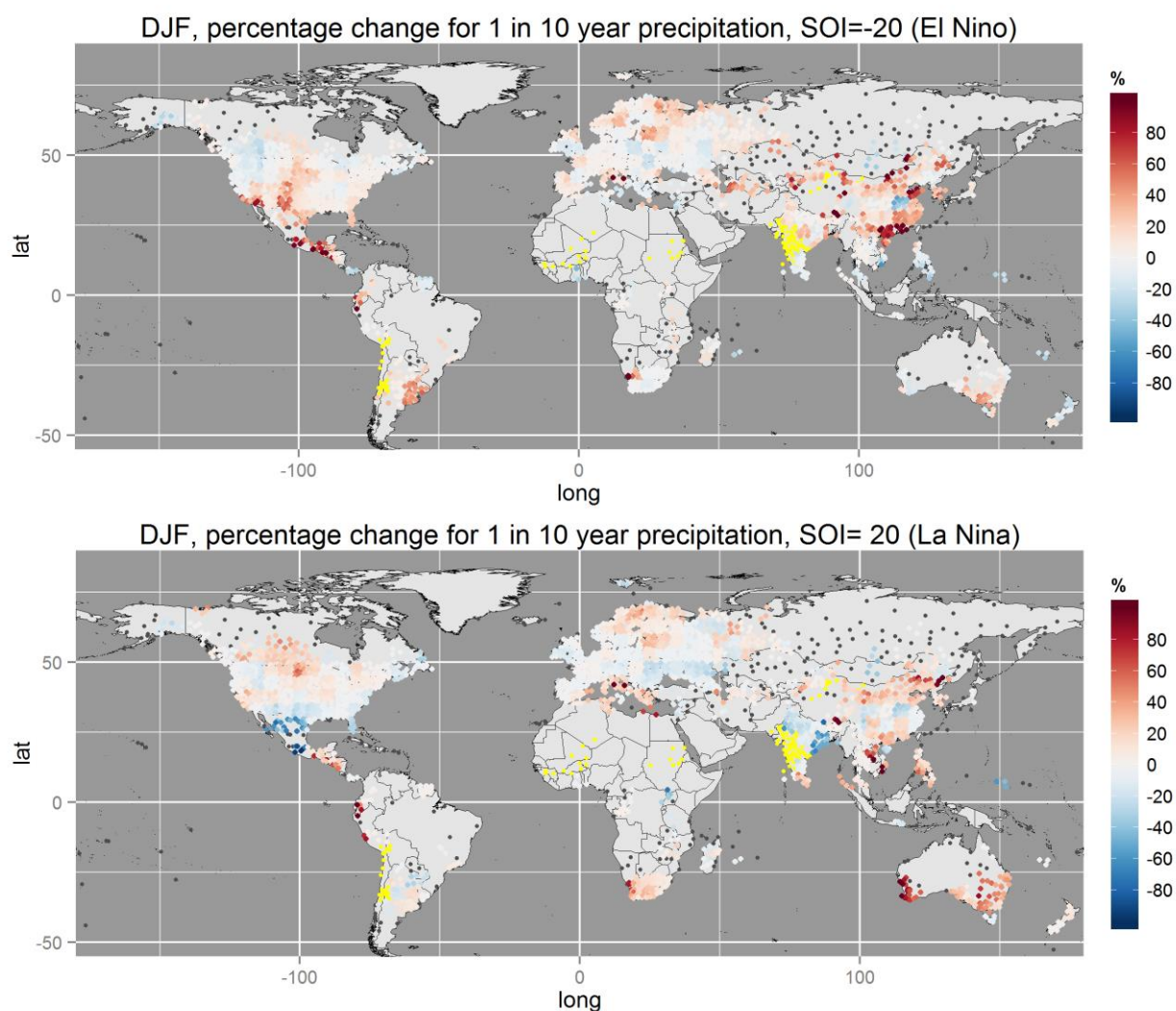
916 **Figure 2: Schematic of observation site selection for each grid cell.**



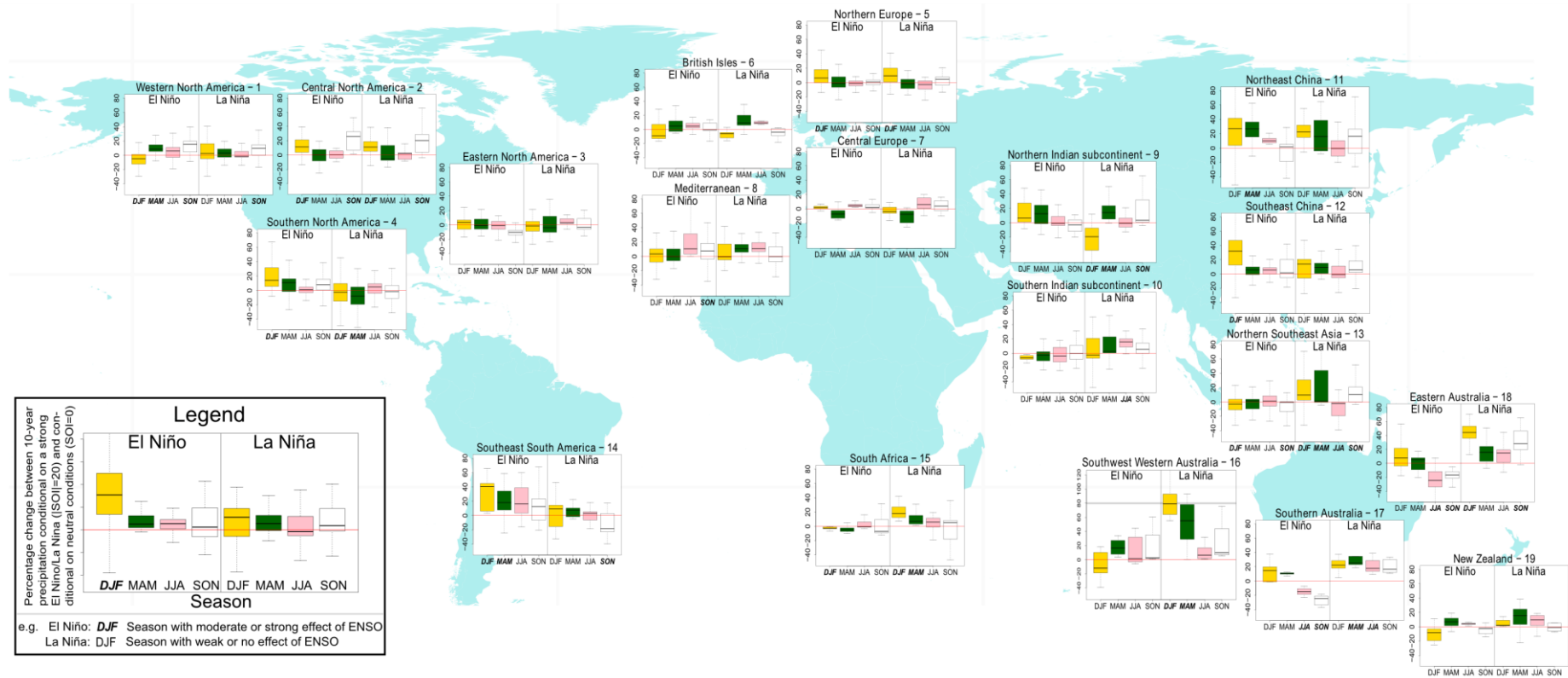
917 **Figure 3: Slope of the location parameter with respect to SOI during El Niño ($\mu_{reg_1}^-$) and La**
 918 **Niña ($\mu_{reg_1}^+$) phases for DJF season. Small grey dots denote cells with too few data stations to**
 919 **perform a regional analysis. Dots with red (blue) outlines denote significantly positive**
 920 **(negative) slopes, while dots with grey outlines denote non-significant slopes. Dots with yellow**
 921 **outlines denote the dry regions with frequent zero precipitation during DJF.**



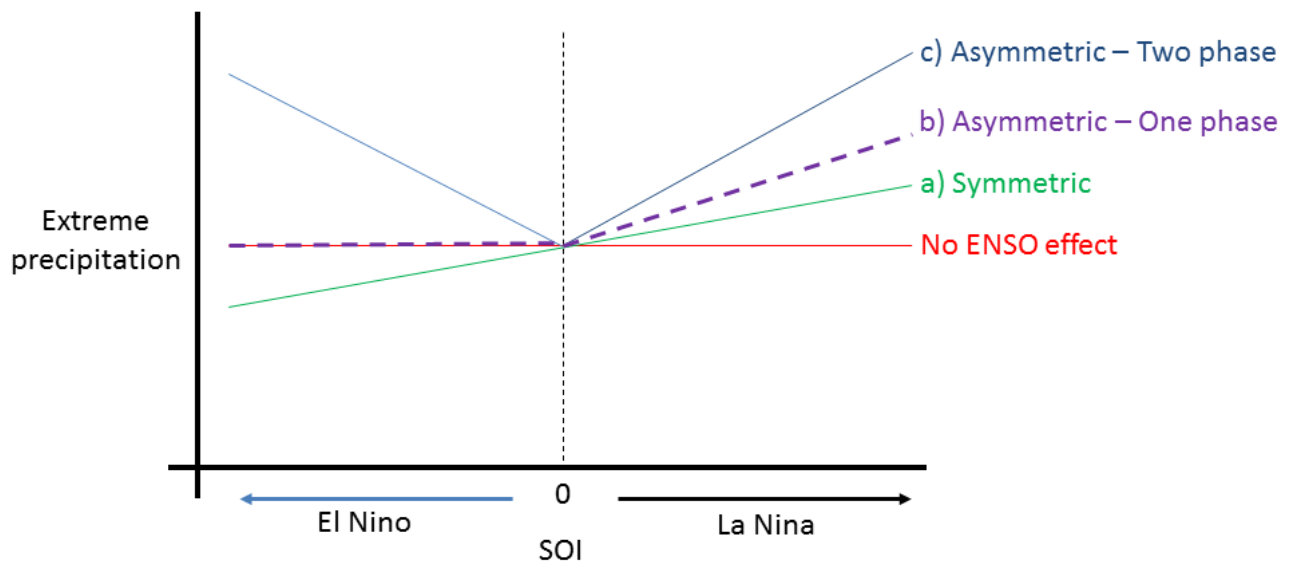
922 **Figure 4:** Same as Figure 3, but for scale parameters $\sigma_{reg_1}^-$ (El Niño) and $\sigma_{reg_1}^+$ (La Niña).



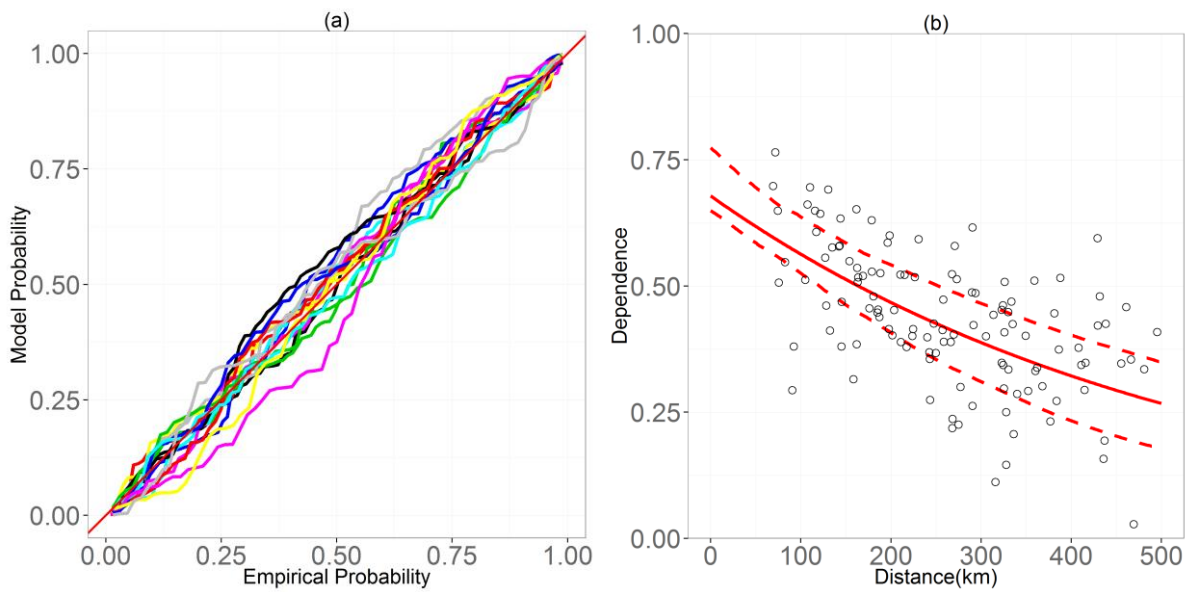
923 **Figure 5: Percentage change for the intensity of 1 in 10 year precipitation relative to SOI=0**
924 **for individual gauge locations for DJF season. Grey dots denote cells with too little station**
925 **data to perform a regional analysis. Red (blue) dots denote an increase (decrease) in the**
926 **intensity of a 1 in 10 year precipitation event for strong El Niño/La Niña phases compared**
927 **with a neutral phase. Yellow dots denote the dry regions with frequent zero precipitations**
928 **during DJF.**



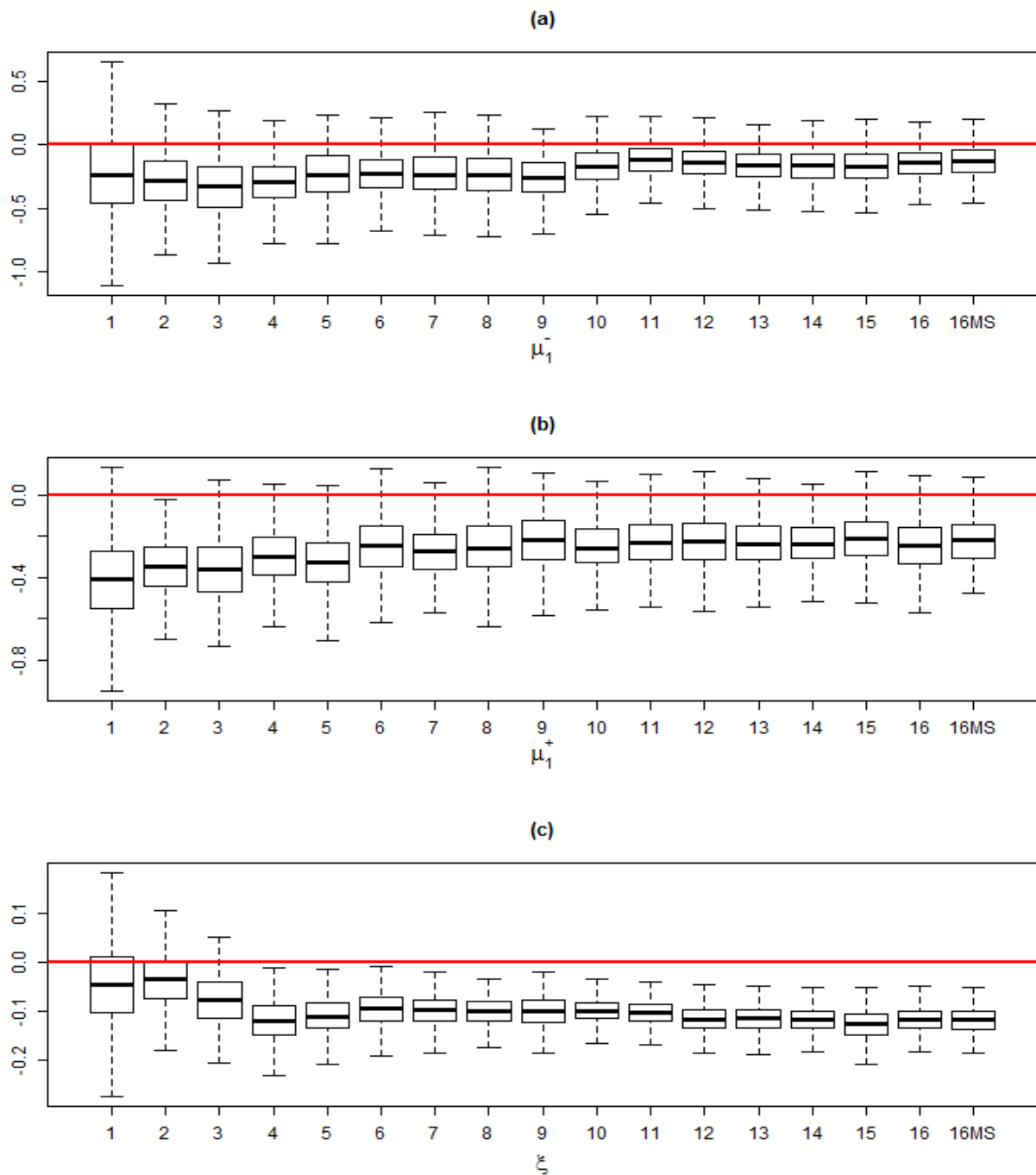
929 **Figure 6: The effect of El Niño and La Niña on the 1 in 10 year precipitations for different seasons. Samples for the boxplot are the**
 930 **percentage change median of the precipitation calculated at each station within the areas shown in Figure 1. The season with moderate**
 931 **or strong effect of ENSO as given by Table 2 is highlighted in bold. (A high resolution figure is available online).**



932 **Figure 7: Conceptual diagram of the types of symmetry/asymmetry in the relationship**
 933 **between ENSO and extreme precipitation. (a) Symmetric relationship: opposite effects in the**
 934 **two phases; (b) One phase asymmetric relationship: no effect for one phase and a strong**
 935 **effect for the other phase; (c) Two phase asymmetric relationship: strong, but non-opposite**
 936 **ENSO effect during both the El Niño and La Niña phases.**

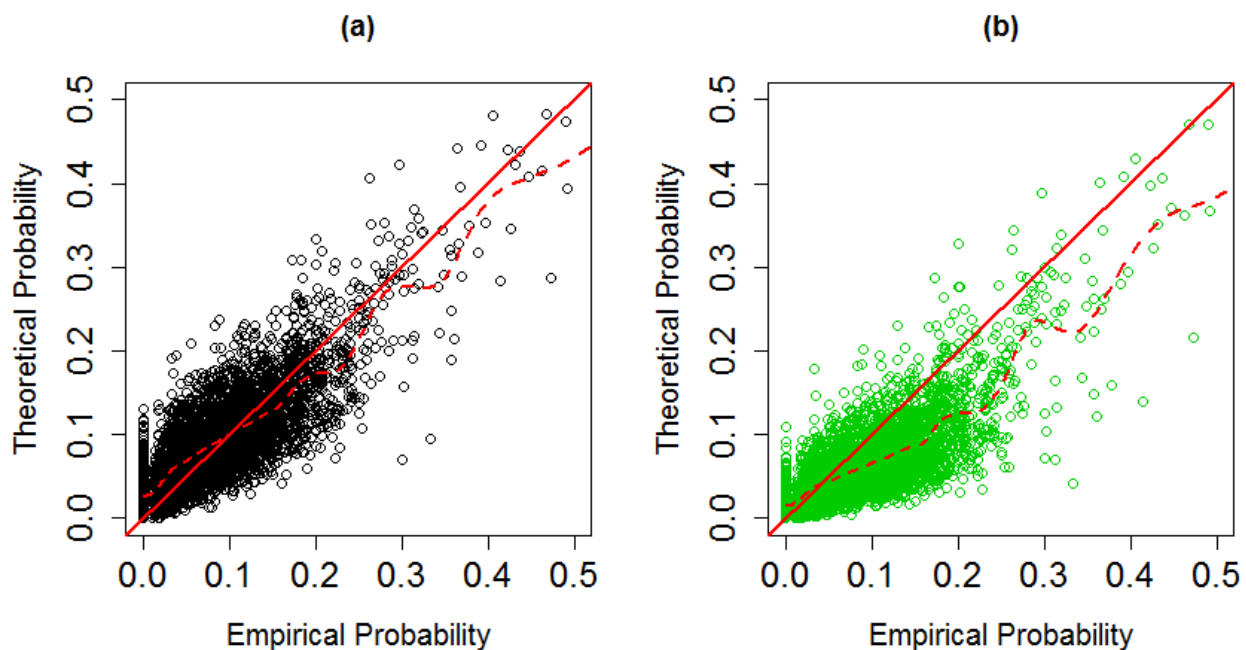


937 **S 1: (a) Goodness-of-fit PP-plot of all sixteen stations. (b) Dependence-distance relationship of**
938 **the Gaussian transformed data. The black dots are the empirical pairwise correlations and**
939 **red lines are the estimation from the exponential model (Eq.(4)) with 90% credibility interval.**



940 **S 2: posterior distribution of the regional parameters $\mu_{reg_1}^-$, $\mu_{reg_1}^+$ and ξ . The first sixteen boxes**
 941 **are the estimation with non-informative priors using from one to sixteen stations. The last box**
 942 **is the estimation using all sixteen stations with Martins and Stedinger' (MS) Gamma(6,9)**
 943 **prior for the shape parameter.**

944



945

946 **S 3: Scatterplot of the probability of a station pair exceeding the 75th percentile of the at-site**
947 **historical seasonal maximum daily precipitation among the stations in a region. (a) Empirical**
948 **probability vs. Theoretical probability calculated by the Gaussian copula model; (b)**
949 **Empirical probability vs. Theoretical probability calculated by the model ignoring spatial**
950 **dependence. The dashed red line is the fit of a cubic smoothing spline.**